In "Structure and Performance of Cements" - P. Barnes (ed) Applied Science Publishers London and New York, 1983

Chapter 4

THE MICROSCOPY OF UNHYDRATED PORTLAND CEMENT

P. BARNES and A. GHOSE*

Department of Crystallography, Birkbeck College, University of London, UK

1. INTRODUCTION

Firstly the chapter title requires some definition. The meaning of Portland cement should be very clear from other chapters of this book; it is sufficient to add that by 'Portland cement' is meant the unhydrated material in clinker form or ground with additives (gypsum, etc.), noting that hydrating and set cements are fully discussed in Chapter 6. However, the standard dictionary definition of microscopy, 'the practice by which objects are magnified to . . .', is hardly sufficient and some personal philosophy from the authors might be more appropriate. A working definition of 'microscopy' devised and adopted by these authors could be, 'the act of direct spatial enlargement of any specimen-contrast phenomena created by the interaction of radiation with the specimen'. This definition, as will be seen, suits the purposes of this chapter, although it too admittedly (and intentionally) has its ambiguities. The word 'spatial' is a key part of the definition; there are indeed many fruitful studies in which the radiative– or particle–specimen interaction can be related to a specific sample site(s) by deduction or surmise, but the lack of a direct spatial relationship renders the act as outside strict microscopy so defined. Examples of ex-definition in cement research could include infra-red, Raman, thermoluminescence, Mossbauer, NMR, etc., although one should note that in principle a scanning mode of

* Present address: Department of Civil Engineering, University of Illinois at Urbana–Champaign, 208 North Romine Street, Urbana, Illinois 61801, USA.

irradiation (e.g. Raman microprobe, x-ray fluorescence) could bring a particular case within the definition.

The most obvious radiations for consideration are visible light and energetic electrons, and together they constitute the major divisions of this chapter. If for convenience diffraction is added to our sights, we can talk logically of imaging real and reciprocal space, for this duality is well suited to the electron microscope; however, considerable difficulty is encountered in utilising x-rays on account of the inherent problems in producing effective x-ray lenses for ordinary imaging. Figure 1 puts the overall philosophy into perspective by considering the microscopy and diffraction from light, electrons and x-rays.

Techniques I, II and IIIa are partly considered in this chapter; IIIb (scanning electron microscope electron channelling), however, has not been found to be sufficiently discriminating for use with highly strained/defective structures as encountered with cements. The x-ray case (IV) is challenging; although crystal structure analysis using either single crystal or powder x-ray diffraction is well established and discussed in relation to cements in Chapter 3, the x-ray microscope has so far been demonstrated in a purely preliminary fashion to a spatial resolution of *c.* 1000 Å and should rather be considered as a more futuristic although interesting possibility (see Section 4). The case of x-ray topography* (IVc) is provocative—the technique unquestionably utilises diffraction, but is it also at the same time microscopy? The argument for microscopy is that a minute feature, such as a single lattice-dislocation† of crystal plane dimensions, is rendered visible on the photographic emulsion while maintaining a direct spatial relationship with the dislocation throughout the crystal. Against this can be argued that the size of the dislocation image is a consequence of the radiation used; for example, a comparison between x-rays (Lang topography) and electrons (dark-field imaging) illustrates the inverse

* X-ray Lang topography is named after Lang[1] who, by extending an earlier technique of Barrett,[2] devised a method for the x-ray scanning of a crystal with the intent of mapping out its lattice defects on the output emulsion film. As shown in Fig. 1, it is operating in the transmission ('Laue') mode. Normal operation requires that the total absorption $\mu t \sim 1$, in which case the full dynamic theory of x-ray diffraction is required to interpret the intensity of main or diffracted beams.

† A dislocation is a linear defect caused by the slippage of part of a crystal with respect to the remainder of the crystal. It is conveniently characterised in terms of a vector ('Burger's vector') which has the units of a crystal plane spacing and is defined by means of a geometrical construction ('Burger's circuit') and comparison with a perfect crystal. The three-dimensional trace of the dislocation defect throughout the crystal defines the dislocation line.

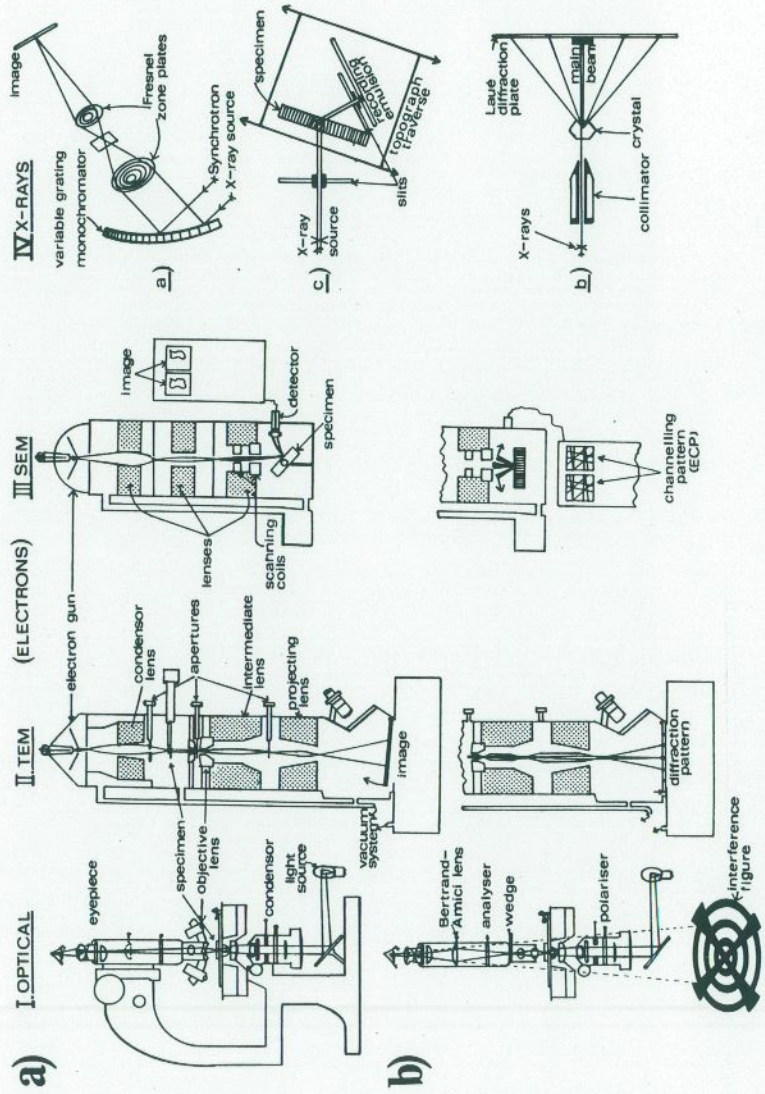

Fig. 1. Schematic illustration of the modes of: (a) imaging, and (b) diffraction-interference, using the radiative properties of (I) light, (II) and (III) electrons, and (IV) x-rays. Such general prospects for the microscopy of cement are discussed in the text.

relationship between sensitivity and resolution—the x-ray diffraction rocking curve of a near-perfect single crystal can be as narrow as 5×10^{-6} rad, producing dislocation image widths of typically $\sim 1\,\mu$m, while electron microscopy yields much sharper < 100 Å image widths. The two radiations simply sample different ranges of lattice strain around the dislocation. Unfortunately, the potentially powerful technique of x-ray topography is not very suited to the study of defects in cement phases on account of the crystal edge effects, high defect densities, and experimental difficulties which dominate with grain sizes less than 100 μm. A less typical cementitious case of a large-formed $Ca(OH)_2$ crystal topograph is, however, given in Section 4.2.

The next two sections deal with optical microscopy and electron microscopy/diffraction, respectively, both techniques having served cement research well.

2. OPTICAL MICROSCOPY OF PORTLAND CEMENT CLINKER

The usefulness of the optical microscope in both routine observation and quality control, and in fundamental cement chemistry research should not be overlooked. An account of some of its past and present uses is given in this section.

2.1. Introducing Optical Microscopy

The history of cement chemistry is indeed strongly linked with optical microscopy; Le Chatelier[3] and Tornebohm[4] are credited with being amongst the first to make extensive use of the polarising microscope to study cement clinkers. Names were coined by Tornebohm (alite, belite, celite, felite and isotropic residue) for the five principal components of cement clinker and, of these five, 'alite' and 'belite' survive to the present day to describe the C_3S and C_2S phases as they occur in cement. The various components of cement can be distinguished with reasonable, but not always complete, certainty from a combination of polarising light microscopy and chemical etching techniques. The interstitial phases, particularly solid solution ranges (see later), are more difficult to distinguish optically. However, by combining electron and optical microscopy we have a more versatile arrangement for the identification of all phases including the determination, with reasonable precision, of the appropriate region of the solid solution range in question. Optical studies

are not limited to research on already standardised systems; Maki and co-workers have, for example, shown how new phases and classifications can be made on the basis of purely optical data, and in particular Maki and Chromy[5] have discovered a new monoclinic ('M3') phase for C_3S in the temperature range 1060–1070 °C, this M3 phase being evident from a large (120 °C) rotation of the optical indicatrix around [0001] although there had been no indications from differential thermal analysis (DTA) or x-ray diffraction (XRD) measurements of any concomitant phase change.

The general optical techniques that are considered here in the context of cement microscopy, are: (1) the study of crystal habit and/or form; (2) the use of chemical etching as a microscopy aid; and (3) the determination of refractive index/indices. The usefulness of the former two should become clear in this section, and for the latter we may refer to the three principal refractive indices n_α, n_β and n_γ, and birefringence, Δn,* for a crystal. Readers who are unacquainted with any of the standard optical techniques are referred to one of many textbooks[6–9] on the subject.

2.2. Optical Preparation

For cement samples in optical studies, three preparative conditions are usually considered; crushed clinker powders, polished sections and thin sections. In general, the preparation details are similar to those described in any mineralogical textbook with obvious regard for the reactivity of cement with water. A gross section of the specimen is easily obtained using a diamond saw. After resin impregnation to fill pores, grinding and polishing is performed with oil-based lubricants/coolants (e.g. lapping oil, ethylene glycol, propylene glycol, liquid paraffin) replacing water and with carborundum, diamond or alumina paste on good cloth (e.g. linen, twill, silk) down to less than 1 μm for the final polish. If it is intended that the sample should subsequently be used in connection with EMPA (electron microprobe analysis) elemental analysis, it is preferable to use diamond paste which does not affect the Si or Al analysis. For thin sections, the procedure is repeated on both sides of the specimen for a final thickness of 20 μm or less, and final mounting on a glass cover slide can be improved

* The terms 'principal refractive indices ($n_\alpha, n_\beta, n_\gamma$)' are for light vibrating parallel to three mutually perpendicular directions defined with respect to crystallographic axes for all seven crystal classes.[10] By convention, $n_\alpha \leq n_\beta \leq n_\gamma$. If: (i) $n_\alpha = n_\beta = n_\gamma$, the crystal is optically isotropic; (ii) $n_\alpha = n_\beta \neq n_\gamma$, the crystal is uniaxial positive; (iii) $n_\alpha \neq n_\beta = n_\gamma$, the crystal is uniaxial negative; and (iv) $n_\alpha \neq n_\beta \neq n_\gamma \neq n_\alpha$, the crystal is biaxial positive when $(n_\beta - n_\alpha) < (n_\gamma - n_\beta)$, and biaxial negative when $(n_\beta - n_\alpha) > (n_\gamma - n_\beta)$. Maximum birefringence, Δn, is defined as $|n_\gamma - n_\alpha|$.

(optically) by use of an optical mounting medium such as Canada balsam hot pressed between the section and slide. If electron microscopy is envisaged, it might be prudent to use a thermosetting resin as a mounting medium for subsequent release, e.g. 'Crystalbond 509' which softens at 130 °C and dissolves in acetone. In the case of crushed powders, optical continuity can be improved with drops of immersion oil (approximately 2:1 methylene iodide and *m*-bromonaphthalene) on the powdered sample. A crushed powder specimen can enable a quick estimation of crystal size and refractive index using transmitted light (see Ono's method, Section 2.6) but not of detailed features or gross features such as porosity and homogeneity. Polished sections are less time-consuming than thin sections and their observation in reflected light can be informative to the trained eye. The observation of polished sections with various chemical etching techniques for phase differentiation is a popular combination. A full optical classification (including birefringence, pleochroism,* etc.) requires the more tedious thin sections which, however, can be viewed in the transmission or reflection mode, and with or without the use of a differential etch.

A fuller description of sample preparation for optical techniques may be acquired from a number of treatises[11–15] on the subject. For the convenience of practitioners, Table 1 summarises a list of the presently known main optical and characteristic features, together with suitable etchants, for the main constituent phases of Portland cement. The potential range of constituents allowing for all substitutional impurities and solid solution effects is infinite, so eight representative constituents are given; these for convenience are referred to symbolically as the silicate phases C_3S (alite) and C_2S (belite), the four interstitial phases C_3A (tricalcium aluminate), C_4AF (known as brownmillerite and being representative of the C_2A–C_2F solid solution range), NC_8A_3 (another extreme of the C_3A–NC_8A_3 solid solution range), the glassy amorphous phases, and finally free-lime (CaO) and magnesia (MgO) aggregations in view of their critical effect on long-term strength[16] due mainly to their adverse expansion to portlandite ($Ca(OH)_2$) and brucite ($Mg(OH)_2$) on hydration.

Figure 2 gives a typical optically polished section of works' Portland

* 'Pleochroism' may be defined as the variation in colour arising from the variation of light absorption (for different wavelengths) with vibration direction relative to the crystal. It can be described using three principal parameters (just as with refractive indices) or more qualitatively by way of the colour variations experienced when rotating the crystal in the polarising microscope with the analyser removed.

cement clinker after etching by boric acid and potassium hydroxide. The principal component of cement, alite (normally 50–70 % of total), is readily distinguished by its characteristic crystallite shape (see Table 1), and is conveniently distinguished from belite (normally 10–30 %) by the different colours (from interference effects or otherwise) in reflected light resulting from the differing surface-etch films on each phase.

2.3. Ordinary Portland Cement (OPC) Alites

The original C_3S XRD structure analysis by Jeffery[35] was based on a pseudo-rhombohedral (R3m)–true monoclinic (Cm) cell. However, C_3S undergoes many minor polymorphic transformations (see Chapter 3) between room temperature and 1100 °C exhibiting at least three triclinic, two monoclinic and one trigonal (rhombohedral) polymorphs (see Table 1). A classic exposition of these polymorphs based on XRD and DTA data has been given by Guinier and Regourd,[36] and more recently modified by Maki and Chromy[5(a)] to take into account their additional 'optical monoclinic (M3)' phase at 1060 °C. The current state of the art is discussed in Chapter 3.

There is still some difference of opinion, because of slightly conflicting XRD and optical data, over which polymorphs occur in cement alites, although it is more generally agreed[20,35,36,41(a)] that the monoclinic forms (probably M1 and M3[18]) are dominant, the commonly observed external pseudo-hexagonal outline of alites in optical sections being merely a 'morphological reminiscence' of the higher temperature trigonal form. The differences in alite optical properties and habit resulting from the kiln burning conditions will be discussed later (see Ono's method, Section 2.6) although some basic observations regarding the optical characteristics of clinker alites are now required. Apart from the usual pseudo-hexagonal shape which has already been mentioned, the inversion textures of alites are generally much less distinctive than those of the striated belites (see Section 2.4), although some polysynthetic twinning and somewhat disputed twinning habits, including three-fold cyclic twinning on the three pseudo-trigonal $\{21\bar{1}0\}$ mirror planes, are observed (see Section 3.4).

Zoned alites (see Fig. 2(f) for a particularly vivid example) were first noticed by Guttman and Gille[37] and were believed[21] to be particularly related to the kiln burning conditions (see later). Chromy[23] demonstrated that this was the result of two different alite polymorphs (and not just differences in solid solution) by showing the inner alite core to be a low-temperature (with lower birefringence) and the rim to be a high-temperature (with higher birefringence) polymorph. Maki and Goto[17]

TABLE 1

OPTICAL PROPERTIES AND CHARACTERISTICS OF COMMONLY OCCURRING ORDINARY PORTLAND CEMENT (OPC) PHASES AND CORRESPONDING PURE SYNTHETIC PHASES[a]

Phase	*Polymorph*	*Refractive index*	*Birefringence*		*Optical Class*	*References*	*Optical characteristics*	*Suitable etchant*
			Pure C_3S	*OPC alites (at room temperature)*				
C_3S/alite	*Pure phases and inversion temperatures*							
	T_1 (triclinic, 0 °C)	1·723	0·002 5		Biaxial-negative	5, 12–15, 17–23, 29	Normally euhedral colourless biaxial crystals of weak Δn. Size range 15–60 μm, invariably with pseudo-hexagonal outline. Easily differentiated from belites by etching.	HF-vapour yields yellow/amber colour in reflected light. Also: ethylene glycol + alcohol, 10 % $MgSO_4$ in water + wash/dry, $\frac{1}{4}$ % HNO_3 in alcohol, 1 % NH_4Cl in water. Other cocktails (see Reference column).
	T_2 (triclinic, 620 °C)		0·002 3	0·003–0·005				
	T_3 (triclinic, 920 °C)		0·002 3					
	M_1 (monoclinic, 980 °C)		0·002 6	0·005–0·006				
	M_2 (monooclinic, 990 °C)		0·002 6					
	M_3 (monoclinic, 1 060 °C)		0·003					
	R (rhombohedral, 1 070 °C)		0·003	0·007–0·010	Uniaxial-negative			
OPC alites (at room temperature)		1·719–1·724		0·002–0·010	Various			
C_2S (pure)	α (hexa/trigonal, 1 420 °C)	1·652–1·713	0·005–0·009		Uniaxial-positive	12–15, 19–24, 29	Belites normally darker and more rounded grains of higher Δn. Size range 5–30 μm, invariably spotted by their characteristic striated structure. The lamellae usually occur in intersecting sets, containing fine polysynthetic twins.	HF-vapour yields blue/red colour in reflected light. Also: 10 % $MgSO_4$ in water, particularly for high alumina cements. Other cocktails (see Reference column).
	α′ (orthorhombic, 720 °C)	1·712–1·716	0·009–0·013					
	β (monoclinic, 20 °C)	1·717	0·018					
	γ (orthorhombic, 20 °C)	1·642–1·645	0·012		Uniaxial			
OPC belites (at room temperature)		1·714–1·735	0·003–0·018		Various			
C_3A	(Cubic, 0 °C)	1·710	0		Isotropic	12, 26, 27(b), 31	Cubic when pure or nearly pure. Easily confused with C_3S (similar optical properties) but noticeably less bright than the C_4AF-interstitial. Sometimes enclosing C_3S and CaO. Other forms in solid solution (see NC_8A_3 and Section 2.5).	Appears dark and crystalline after distilled water etch. Also: 1 % HNO_3 in alcohol.
C_4AF	(Orthorhombic)	1·94–2·08	0·10		Biaxial-negative	12, 19, 27(b), 29, 30, 32, 34	Usually in prismatic form, often as small needle-shaped prisms. Sometimes recognisable by reddish colour and brightness. High n and Δn; exhibits pleochrism.	10 % NaOH solution (+wash) to differentiate ferrites (unaltered) and aluminates (dark blue). Water + alcohol followed by $\frac{1}{4}$ % HNO_3 + alcohol if Fe content is low.
NC_8A_3	(Prismatic)	1·710–1·717	0·008		Biaxial-negative	12, 27, 31	Thin tabular crystals with complex polysynthetic twinning. Other forms in solid solution (Section 2.5).	Water followed by 1 % HNO_3 in alcohol, then distinguish from C_3A by form.
Glass	(Amorphous)	≥ 1·72	0		Isotropic	12–15, 24, 25, 29, 30	Colourless dark phase of high n and zero Δn.	High Fe-glasses: $\frac{1}{4}$ % HNO_3 + alcohol, or 10 % KOH + water. Low Fe-glasses: etch as for C_3S.
CaO	(Cubic)	1·836	0		Isotropic	12–15, 29, 30, 33	Occurs as aggregates or rounded grains, sometimes up to 20 μm size. Sometimes embedded in C_3A, C_3S and C_2S. In polished sections is often recognised by its easily scratched surface due to its softness.	White's reagent = 5 g phenol in 5 cm^3 NB. + drop of water—yields distinctive calcium phenoxide crystals but cannot distinguish CaO and $Ca(OH)_2$. Also: ethylene glycol + alcohol and distilled water.
MgO	(Cubic)	1·736	0		Isotropic	12–15, 30	Usually occurs as small angular (rectangular or triangular phase) bright grains. Stands out in high relief on polished surface due to its hardness. Sometimes occurs as inclusions as with CaO.	Not affected by normal etchants.

[a] Various polymorphic schemes are in use (see Chapter 3); for simplicity the optical classification of Maki[5,27a] (C_3S, C_3A + N) and powder XRD classification of Barnes *et al.*[28] (C_2S) are used here, the lower inversion temperature being quoted. Refractive index, n, refers to the ordinary component, n_ω, where this is unambiguous, otherwise a mean value is given; birefringence, Δn, refers to the maximum value measured which should correspond to $|n_\gamma - n_\beta|$. It should be noted that the pure C_3S data are given for inversion temperatures appropriate for each phase since extrapolation of data to room temperature is not possible in every case. The clinker data, however, all refer to the room-temperature stabilised product. Where there are diverse values in the literature, the preferred value(s) is underlined. Some interpretation by the authors is inevitable.

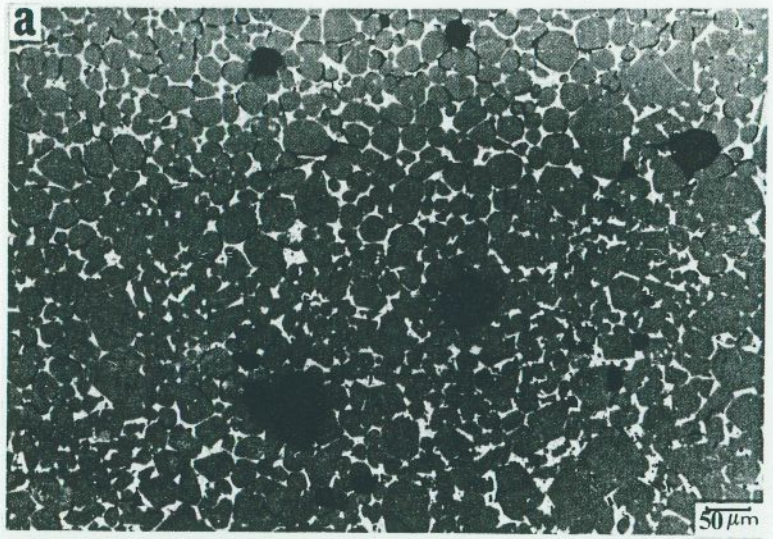

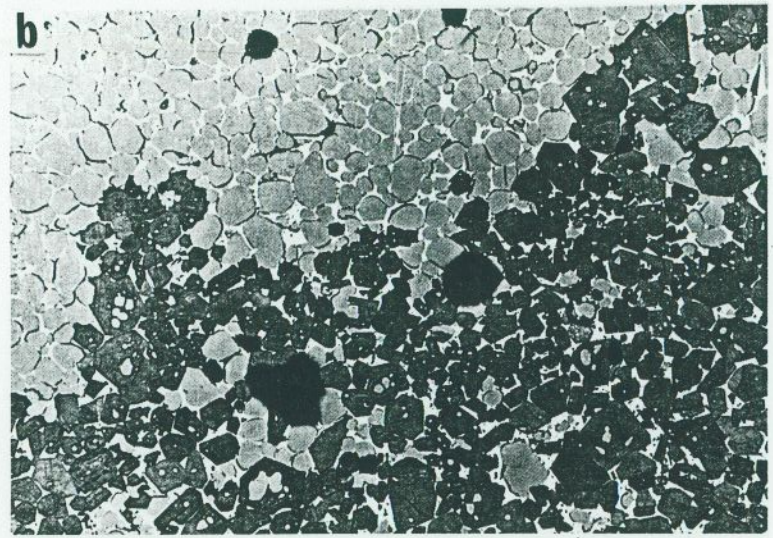

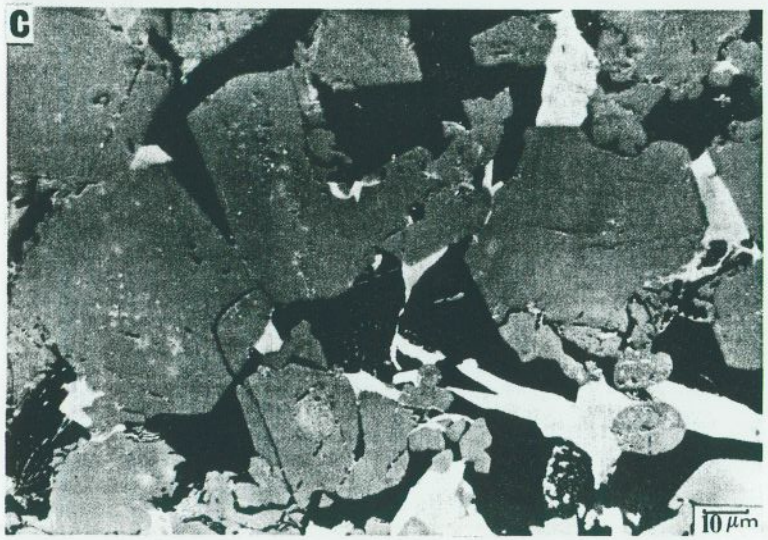

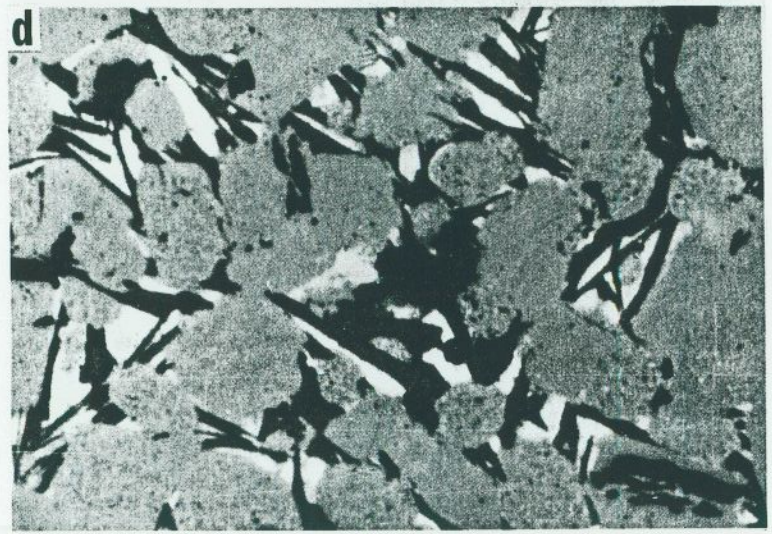

Fig. 2. (a)–(d). Optical micrographs of polished surfaces of normal Portland cement, illustrating the effects of chemical etching: (b) is of the same area as (a) but is shown after etching with 10 % boric acid in water to bring out the silicate (light grey—C_2S; dark grey—C_3S) and interstitial (white) phases (the scale on (b) is the same as that on (a)); (c) and (d) show the result of 10 % potassium hydroxide etch to yield black C_3A, grey silicate, and white ferrite phases—note the more normal cubic form of C_3A in (c), and more prismatic shape (alkali absorption) in (d) (the scale on (d) is the same as that on (c)). (Photomicrographs (a)–(d) by courtesy of R. M. Grove, Cement and Concrete Association, Slough, UK.)

Fig. 2. (a)–(d)—*contd.*

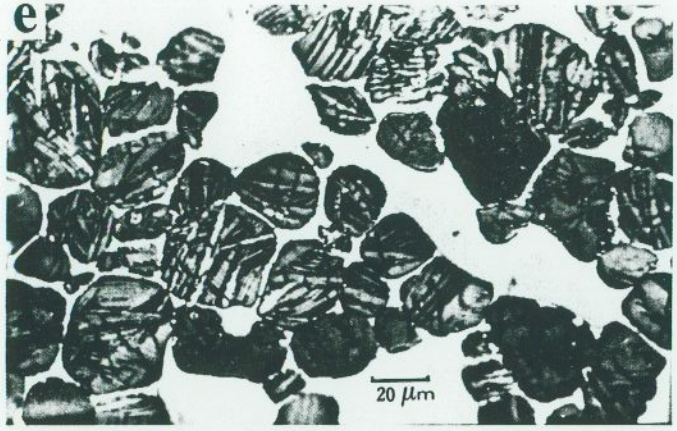

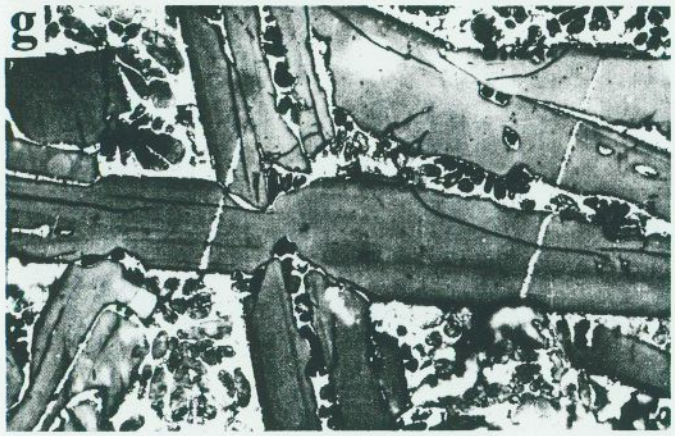

Fig. 2. (e)–(h). Optical micrographs showing less common features of Portland cement: (e) and (f) (scales the same) are of clinker with mineraliser,[87(a)] revealing well-developed belite lamellar structure in (e), and beautiful zoning in alite crystals in (f); (g) and (h) (scales not given) are of fused Portland clinker[90(d)] etched with 1 % HNO_3 to reveal elongated alite crystals in (g); and alite crystals with inclusions of

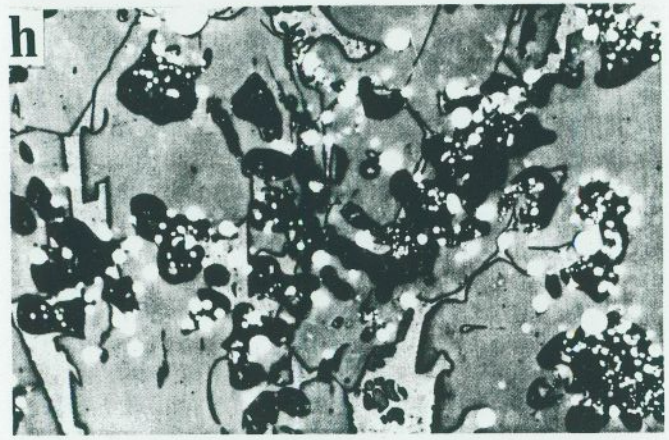

Fig. 2. (e)–(h)—*contd.*

free calcium oxide and iron in (h). (Photomicrographs (e)–(h) by courtesy of the International Cement Microscopy Association, Texas, USA. Prints for (e) and (f) by courtesy of Hargrave *et al.*[87(a)] and for (g) and (h) by courtesy of Wieja and Wieja.[90(d)]

have claimed to have narrowed the choice of these two polymorphs to be the M1 and M3 monoclinic phases, respectively. A simple and plausible explanation for the occurrence of zoned alites is that the outer rim becomes low-temperature form-stabilised by absorbing impurities from the surrounding melt, especially with long high-burn conditions.

2.4. OPC Belites

Belites, the second most abundant (10–30 %) phase in Portland cement, are easily distinguished optically by their normal appearance—darker, normally slightly smaller and rounded grains (yellowish in transmitted light), invariably with characteristic striation patterns—and easily differentiated from alites by chemical etching (see Table 1 and Fig. 2). The striated patterns also become more visible with the use of etching techniques. Insley[29] sub-classified belites into three types (types I, II and III), mainly on the basis of whether the evident lamellae were complex (at least two sets—type I), simple (only one set—type II) or absent (type III). Type I is by far the most commonly occurring form in Portland cement, type II textures being variously associated in some way with the α'-phase, possibly by virtue of an $\alpha' \rightarrow \beta$ inversion, the higher α-phase not being formed in a lower-temperature burn. The origins of the complex intersecting lamellae of type I belite are not certain with many alternative schemes[12,14,19,21,22,32,34–6,38–41] for combinations of the $\alpha \rightarrow \alpha'$, $\alpha \rightarrow \beta$, $\alpha' \rightarrow \beta$, and $\alpha \rightarrow \alpha'$ plus $\alpha' \rightarrow \beta$ inversions; whether the fine banding is true polysynthetic twinning* or a mixture of different polymorphs or phases is also uncertain. On these points, the electron microscopy/diffraction studies of Jelenic *et al.*,[39] Ghose and Barnes[40] and Groves,[41] discussed in Section 3.4, are more revealing and unambiguously support the twinning hypothesis (probably as a direct $\alpha \rightarrow \beta$, martensitically aided transformation[41]) in explaining the type I structure. Electron microscopy indicates three levels of striation structure: gross lamellae features which are easily evident optically; fine polysynthetic twinning bands 0·1–0·3 μm thick (barely visible optically); and an even finer sub-striation structure $\ll$ 0·1 μm thick (invisible optically) which is discussed further in Section 3.

In ordinary Portland cement the predominant belite is believed to be the stabilised β-polymorph, then the α-polymorph, with the α'-form less commonly present, if at all, and fortunately the weakly hydraulic[42] and

* 'Polysynthetic twinning' is a condition in which regular repetition of twinning occurs with parallel twin planes, each alternate twin maintaining the same orientation (see Fig. 20(a) later). The individual twins are usually microscopically thin plates, the overall form appearing to be that of a single polysynthetic crystal.

deleterious low-temperature γ-polymorph being completely absent. It is useful to understand and to be able to control the stabilisations of different belite polymorphs in Portland cement since the evidence[32,34,39,43–59] suggests that differently stabilised belite polymorphs exhibit greater differences in hydraulicity than do the corresponding different alite forms. On simple thermodynamic grounds one expects that the high-temperature pure C_2S α-polymorph would exhibit the greatest reactivity but, in practice, the theory is complicated by the differing stabilisers used (e.g. B_2O_3, P_2O_5, K_2O, BaO, etc.), the differing concentrations of these stabilisers and their effect in promoting different crystal defect densities which, in turn, will affect the hydraulicity and strength, particularly in the early hydration stages—indeed opposite conclusions from different stabilisations are evident in the literature. The use of belite optical studies is also considered later (Section 2.6) with regard to 7- and 28-day strength predictions of Portland cement used in concrete.

2.5. The Interstitial Phases in OPC

The remaining (10–25 %) Portland cement clinker phases can be conveniently grouped together as the interstitial phases, although this broad term embraces several important phases and solid solution ranges. Bogue[12(a)] used four terms to describe the interstitial phases: 'rectangular dark interstitial' (crystalline C_3A); 'prismatic dark interstitial' (probably NC_8A_3 or similar); 'dark amorphous interstitial' (glassy alumino-ferrites); and 'light interstitial' (C_4AF or similar). With several solid solution ranges evident in cement, interstitial phase identification can prove difficult by either optical (see Table 1) or electron–optical means (see Section 3.2) alone.

The dark interstitial phase, embracing C_3A and various solid solutions (see below) and easily confused optically with C_3S, may be recognised by its rectangular (or square) or prismatic-looking outlines, and of course its rapid etch with water. It occurs prominently in the interstitial matrix surrounding the silicate phases with a wide size range (which is inversely dependent on cooling rate) and can also occur in the prismatic form with overgrowths or less commonly with oriented alternations of the ferrite phase, or zoning with variations in Fe_2O_3 concentration; Maki[27(b)] has described some of the morphologies which occur.

The basic C_3A phase, however, first deserves discussion. The structure of pure C_3A was first unambiguously solved by Mondal and Jeffery[60] in 1974. It shows a somewhat unusual $C_{72}A_{24}$ cubic unit cell (space group Pa3) in which the one-eighth times smaller pseudo unit cell (C_9A_3) displays

distorted oxygen octahedral arrangements with ten cavities occupied by nine Ca^{2+} ions and one unfilled hole (see Chapter 3). This highly strained structure might account for some of the properties of C_3A, such as its high reactivity with water and its complex lattice substitutions[61] (e.g. by Na, K, Fe, Si) in which the unfilled (by Ca^{2+}) hole undoubtedly plays a significant part. In commercial cement, these various solid solutions are all important in promoting other structural forms; in particular, Maki[26,27] has made a deeper study of the $C_3A + N$ system up to NC_8A_3, this system being collectively termed 'anisotropic' or 'dark interstitial' C_3A:

Chemical range;	0–1·6%N	3·8→5%N	5–6·2%N	NC_8A_3
Structural designation	Cubic	Orthorhombic	Monoclinic	Prismatic
$C_3A + N$ system	All room-temperature phases, after Maki[27(a)]			

'Rectangular' or 'crystalline dark interstitial' and 'prismatic dark interstitial' become, respectively, the names for the extreme members of this system. Maki[26] has studied the optical properties of this anisotropic $C_3A + N$ system, and has shown them to be sensitive to compositional changes exhibiting marked birefringence–dispersion and clear optical indications (birefringence) of polymorphic transformations at higher temperatures (e.g. monoclinic to orthorhombic at 500 °C). In Portland cement, all forms (cubic, monoclinic, orthorhombic, prismatic), disputedly,[27,62,63] occur with the cubic and orthorhombic being the most common forms.

The remaining two interstitial phases ('dark amorphous glassy' and 'light' alumino-ferrites) are generally less affected by chemical etch techniques, and the considerable range in composition of both is accompanied by changing optical properties.[64] Of the two, C_4AF is far more easily distinguished due to its high reflectivity (hence 'light' interstitial) and marked pleochroism. According to Chaterjee[32,34] the range of solid solutions encountered in UK, USA, French, Russian and Indian cements is mainly $C_4A_{0·67}F_{1·33} \rightarrow C_4A_{1·33}F_{0·67}$ with the mean close to C_4AF. The glassy phase is characteristic of rapid clinker cooling and, with its reflectivity and etching behaviour being very composition-dependent, is somewhat difficult to identify optically. The range of compositions involved makes the technique of electron microprobe analysis (EMPA) particularly appropriate to these phases, and this is discussed further in Section 3.2.

2.6. The Ono Method

A good example of optical techniques used in everyday cement production has been established by Ono[20,21(a),22] based on over 10-years analysis of a Japanese cement works (Onoda Cement Co., Tokyo) in what has become known as the 'Ono method'. The technique is relatively simple and fast (up to 10 min per sample), involving optical characterisations of alite and belite grains in representative pulverised powder samples, birefringence being estimated from the interference colour and crystal thickness relationship given by the well-known Michel–Levy scale of birefringence (see Reference 12(b), for example). The technique is aimed at providing a rule-of-thumb prediction of cement quality from optically measured parameters; it assumes that additional factors, such as raw mix contents, and free CaO and MgO contents, are already well controlled. By using longer-term (28 days) strength as the key parameter for cement quality, complications from many factors, such as particle size and distribution, alkali/sulphate content, solid solution with C_3A,[27(a)] and crystal defects and impurities in the C_3S, C_2S and C_3A lattices all of which are known[39,43,44,47,49,52,54,55,65–77] to affect early strength, can be avoided. The basic premise of Ono is that four main factors which influence cement quality can be effectively indicated from four optical measurements on cement clinker powder. These are:

1. Heating rate (1200–1400 °C)—indications from *alite size*: the chief (inverse) relationship is that a slow cooling rate (particularly 1200–1300 °C) encourages larger and coarser C_2S and CaO growth with the succeeding alite formation being slower, i.e. alite crystals are fewer but larger.
2. Maximum temperature—indications from *alite birefringence*: the birefringence of alite is a function of many factors such as impurities, solid solution, polymorph and temperature. Rather than referring to the pure C_3S high-temperature data (Table 1), one must consider the birefringence of typical cement alites at room temperature which reflects the maximum temperature by virtue of the relationship with the alite form stabilised viz: high-temperature form (trigonal), $\Delta n = 0·007–0·010$; intermediate (monoclinic) forms, $\Delta n = 0·003$(M1) and 0·005–0·006(M3); and low-temperature (triclinic) form, $\Delta n = 0·005–0·006$.
3. Keeping time (at 1400 °C)—indications from *belite size*: the belite size also depends on many factors, including raw mix contents, and also increases with keeping time—at low temperatures growth by

cannibalism is small but increases significantly above the $\alpha \rightarrow \alpha'$ transition (1350–1400 °C).

4. Cooling rate (1400–1000 °C)—indications from *belite colour*: the colour/birefringence of belite decreases with temperature due to the differing stable polymorphs (see Table 1), whilst the solubility of various impurities increases with temperature. The cooling rate affects the final proportions of α- and β-C_2S (α' mostly absent) and unexsolved impurities, and these factors, in turn, affect the hydraulicity (see Section 2.4). The colour varies from colourless (fast cool, high α-C_2S content, low Δn) to yellow or amber (slow cool, lower α-C_2S content, higher Δn).

These four factors combine to yield an overall 28-day strength classification which is optimised when conditions encourage a high-temperature burn for sufficient time followed by a quick cool. The overall relationships between burning condition, alite/belite habit, and 28-day strength are summarised in Table 2 derived from the work of Ono.[20,22]

On balance, the Ono method has received mixed reactions[11(a),17,78–86] regarding its predictive powers, although its largely qualitative nature should not be overlooked. Some discrepancies no doubt arise through its incorrect application, and others simply because no single kiln is truly typical of all kilns. It has been favourably used by some as a 'trouble-shooting' aid (e.g. for a kiln start-up) while others have sought to extend the technique by using extraction aids and CaO content measurement, although the technique is then no longer a quick method.

2.7. Other Optical Classifications

Several cement manufacturers invest in more detailed optical analyses of their works' raw mix feed[11(b),85,87] and normal[11(a),16(b),16(d),17,30,32,34,88,89] and trial[16(a),90] cement outputs. In addition to the four basic observations central to the Ono method, more detailed observations are made in practice. For example, in addition to Ono's single parameter belite colour for judging the cooling rate, other observable factors such as the development of alumino-ferrite phases (fine flux structures or glassy phase with rapid cool), and the size/distribution of CaO and MgO, belite fringing on alite grains, and C_3A size/crystallinity are all indicators of slow cooling (see Figs 3(a), (b) and (h)). To quote one case, Long[88(b)] has investigated Portland cement from the Northfleet (UK) works with a view to identifying six major factors (burning regime, cooling rate, composition, raw feed preparation, blending, reduction environment) mainly from the size and

TABLE 2

RELATIONSHIPS BETWEEN BURNING CONDITION, ALITE/BELITE HABIT AND 28-DAY STRENGTH; DATA TAKEN FROM THE WORK OF ONO.[20,22] ALTHOUGH OTHER VARIABLES ARE INVOLVED, THE GENERAL TRENDS ARE ILLUSTRATED WITH REGARD TO THE FOUR OPTICAL MEASUREMENT PARAMETERS LISTED

Burning conditions:	*Excellent*	*Good*	*Average*	*Poor*	
Typical 28-day strength (psi):	*5 940*	*5 670*	*5 000–4 860*	*4 860–4 600*	*4 050*
Burning rate:	Quick			Slow	
(1) *Alite size (μm):*	15–20	20–30	30–40	40–60	
Maximum temperature:	High			Low	
(2) *Alite birefringence:*	0·010–0·008	0·007–0·006	0·006–0·005	0·005–0·002	0·002
Burning time:	Long			Short	Overcharge and flash
(3) *Belite size (μm):*	40–25	25–20	20–15	10–5	
Cooling rate:	Quick			Slow	
(4) *Belite colour:*	Clear	Faint-yellow	Yellow	Amber	
Belite birefringence:	0·012	0·015	0·017	0·018	
α-C_2S content (%):	40	20	10	0	

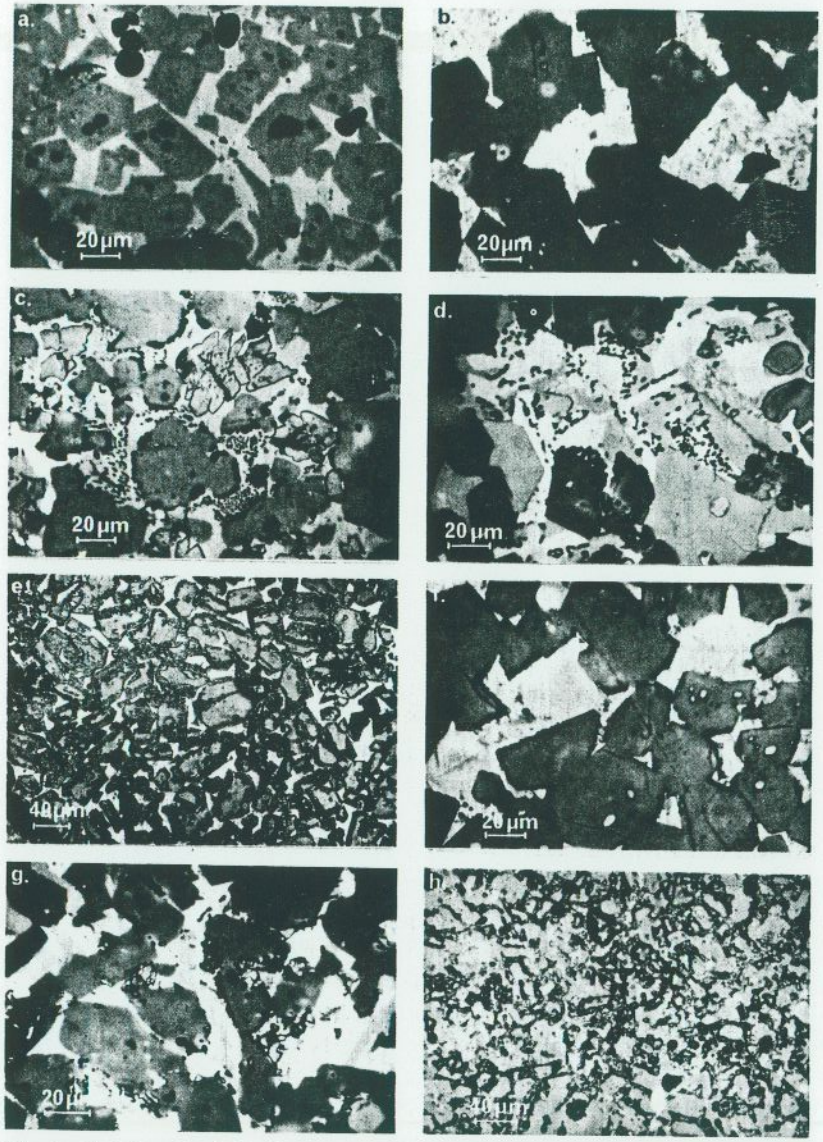

Fig. 3. (a)–(d). Optical micrographs illustrating some effects of different cooling rates on the clinker structure: (a) water quench—retains liquid phase as a glass; (b) rapid cool—fine flux structures; (c) slow cool—large aluminate and ferrite crystals and belite fringing on alite; and (d) slow cool—large periclase crystals. (e)–(h). Optical micrographs illustrating some effects of non-standard burning temperature—environment conditions: (e) maintaining at 1200 °C—alite degraded to intimate belite/free-lime mixture; (f) reducing environment; (g) reduced, slow cooled—alkali-modified aluminate phases; (h) reduced, quickly cooled. (All photomicrographs reproduced with permission from the International Cement Microscopy Association, Texas, USA; prints (a)–(h) by courtesy of G. Long[88(b)] of Blue Circle Technical (Research Division), Greenhithe, UK.)

distribution of alite, belite and CaO phases. The authors have included some optical micrographs from this work in Fig. 3 which illustrates some examples of 'optical trouble shooting'.

A further extension of cement microscopy to include electron microscopy has been referred to several times already; the optical and electron microscopes complement each other well in the field of unhydrated cement clinker, and so electron–optical and allied techniques will now be discussed.

3. ELECTRON MICROSCOPY OF UNHYDRATED CEMENT

Electron microscopy has undergone continual changes and improvements over the last two decades, unlike optical microscopy which, whilst still finding use in fundamental cement research, is still substantially the same—technique wise—as that practised some 50 or more years ago. In addition to the superior resolution of electron microscopes over optical systems, there is the additional capability of extracting structural (micro-electron diffraction) and chemical (electron microprobe analysis (EMPA)) information, and not surprisingly cement researchers are increasingly using electron–optical methods in their work. The four most significant changes in electron microscopy are: (1) the improvement of the resolution of transmission electron microscopes (TEM) to the present 1–3 Å level; (2) the harnessing of higher voltage microscopes (HVTEM) to 1 MeV and above; (3) new specimen thinning and preparative techniques; and (4) the increasingly more powerful and versatile scanning electron microscopes (SEM). Cement research has benefited from all of these changes although perhaps not to the fullest extent possible (see Section 4), and so it is more appropriate in the context of this book that recent examples of electron microscopy are considered rather than a review of the historical aspects of the subject. Several books[91–102] deal with the general theory and operation of electron microscopes and the reader may wish to refer to these for basic information on cement microscopy. The aspects of the present

use of electron microscopy for the study of unhydrated cement will be considered in four sections (SEM, EMPA, TEM + MA, ED).

3.1. Scanning Electron Microscopy (SEM)

The basic SEM was introduced by the Cambridge Instrument Company (UK) in the early 1960s; its basic mode of operation is illustrated in Fig. 1(IIIa) and several books[91-102] exist on it. The resolution (~200 Å) and depth of field of even the earliest instruments were one to two orders of magnitude superior to those of optical microscopes while the modern SEMs possess resolutions typically of 50 Å or better which is better than that needed for most bulk cement studies. Specimen preparation for SEM study is also covered in text books; the simplicity of preparation, compared to TEM specimens, is another attraction of the SEM. Samples must be prepared with greater care (in a similar fashion to those for optical sections) when *accurate* microanalysis (see Section 3.2) is desired, whereas for topological studies one simply coats the surface of interest with an electrically conducting layer (e.g. 1–200 Å of carbon, gold, etc.) to earth to prevent surface charging under normal SEM viewing. The SEM has been most extensively used in hydration studies (Chapter 6), although here we will restrict our attention to the study of unhydrated cements.

Electron microscopy has been used by a number of workers for overall phase characterisation of cements, although with the SEM the additional aids of specimen etching and x-ray fluorescence analysis are powerful tools (see later). Regarding microstructural studies (i.e. intraphase studies), we should first mention the work of Sakurai *et al.*[70] who studied dislocations in crystals of C_3S doped with Cr_2O_3 in an effort to correlate defects with hydraulic activity. They etched polished C_3S sections with various etchants and observed etch pits which were trigons, hexagons and their pseudomorphs, although the etch pit shapes could not be correlated with the crystal symmetry; it was found that the etch pit densities increased with increasing amounts of Cr_2O_3 reaching a maximum of $10^8/cm^2$. Both grain boundary and screw dislocations were observed although it was concluded that only the screw dislocations are active hydration sites. More specifically to SEM, Yamaguchi and Takagi[38,103] and Skalny *et al.*[104] performed SEM studies on partially and selectively dissolved cement clinkers. Some clinkers were found to contain substantial amounts of belite particles embedded in larger alite crystals. These belite particles often had shells of the alumino-ferrite interstitial material around them, suggesting that they were engulfed by alite during crystal growth. The interstitial matrix was studied by dissolving out the silicates with malic acid.

Morphology–composition correlation in the interstitial phase was, however, only partially successful. The interstitial phase was found to have a wide variety of morphologies.[104] Mander and Skalny[105] also used SEM microanalysis to identify calcium and alkali sulphate phases in clinker. Wojnarovits and Udvardi[106] studied the interstitial phase in clinkers by SEM methods and found the interstitial glass to have fully crystallised on heating the clinker to 1400 °C and subsequent cooling. Gouda and Bayles[16(c),107-9] studied the effects of raw materials and processes on clinker formation and reactivity, and concluded that SEM examination of clinkers (alite, belite phases, free-lime content) gives a good insight into the thermal history and the reaction of the raw mix components. They also observed that MgO agglomerates amongst the solid and liquid clinker phases in such a way that the cooling process affects the periclase crystal size and distribution in the interstitial matrix. Regarding clinker grindability under various process conditions, SEM studies have revealed that alite crystals, unlike gypsum, are difficult to grind down in size if overburned when they form large agglomerates. Hornain and Regourd[110] used the SEM to study cracking and grindability of clinker. C_3S was found to be the most brittle, C_2S being much more deformable while C_3A and the alumino-ferrites were the hardest. This order appears to be preserved at the molecular-sputtering level as shown by the ion-etching studies of Barnes and co-workers.[111,112] Matkovic and co-workers[51,113,114] used SEM methods to characterise various doped dicalcium silicates. Both $BaSO_4$ and P_2O_5 stabilise β- and α'-C_2S depending on the level of addition, the higher levels stabilising α'-C_2S preferentially. Present in excess, $BaSO_4$ remains unreacted as a separate grain boundary phase. The shape and size (2–20 μm) of belite grains were found to depend more on the content than on the kind of stabiliser. Papers by Chatterjee[115] and Grattan-Bellow *et al.*[116] draw attention to various operational and instrumental factors, e.g. preparative techniques, surface charging and coatings, image interpretation, etc., that an operator should be aware of when using an SEM in cement studies.

3.2. Electron Probe Microanalysis (EMPA)

In this section we shall cover both the classical electron microprobe method, which uses crystal spectrometers to analyse the characteristic x-rays generated from a specimen under electron bombardment, and the more recent SEM-energy dispersive spectrometer (SEM–EDS) system, which is basically an SEM fitted with a solid-state Si(Li) detector for x-ray

analysis. The purists prefer the dedicated electron microprobe for accuracy of analysis; however, it has been shown that the SEM–EDS system is capable of adequate accuracy. The chief advantages of the solid-state detector are: (1) much higher rate of data acquisition because radiation from all elements is detected simultaneously rather than sequentially; (2) rapid visual display of the spectrum; (3) high collection efficiency; (4) less sensitivity to x-ray source position than crystal spectrometers; (5) a single detector covers a much larger x-ray energy range (1–50 keV); (6) the variable shape and size of a detector helps in interfacing with a host of auxiliary instruments; (7) no moving parts in the spectrometer—hence no wear and tear; (8) a small (as low as 1 cm) working distance between specimen and detector so that lower probe currents can be used to give acceptable x-ray counting rates and hence less specimen damage; and (9) since crystal diffraction is not involved, problems of higher-order diffracted lines interfering in the spectrum are eliminated. Against these, the chief drawbacks are: (1) lower energy resolution; (2) lower sensitivity; (3) inability to detect elements lighter than carbon ($Z = 6$) in principle because of the inherent low-energy electronic noise in the system, and for normal practical purposes elements lighter than fluorine ($Z = 9$) because of the protective Be window on the detector; and (4) permanent liquid-nitrogen cooling for the detector. The reader is referred to standard treatises for more detailed information on methodology and instrumentation.[102,117(a),118]

One of the advantages of the SEM–EDS system over the dedicated microprobe is that secondary electron imaging of surfaces as performed with the SEM normally yields a better picture resolution than that of the back-scattered mode of imaging as generally used in microprobes.[102] Both systems are, however, capable of generating x-ray maps, element by element, as a valuable aid to phase delineation. Accurate (quantitative) x-ray work calls for very flat specimens having the minimum surface relief thereby minimising spurious x-ray generation arising from interference between back-scattered electrons and any surface protuberances alongside the area of interest. Local surface tilt and x-ray take-off angles are also measured more accurately with a flat specimen. Hence highly polished specimens (preferably down to 0·25 μm diamond paste) are required, as shown in Fig. 4(a) with Fig. 4(d) being the corresponding Fe x-ray map. The bright areas are rich in Fe and correspond to the interstitial phase whereas the dark areas correspond to alites and belites. Elements present in smaller amounts (<5–10%) yield poor x-ray maps because of the low peak ('signal') to background ratios. Also, small differences in elemental concentration are not readily revealed with x-ray maps, so that, for

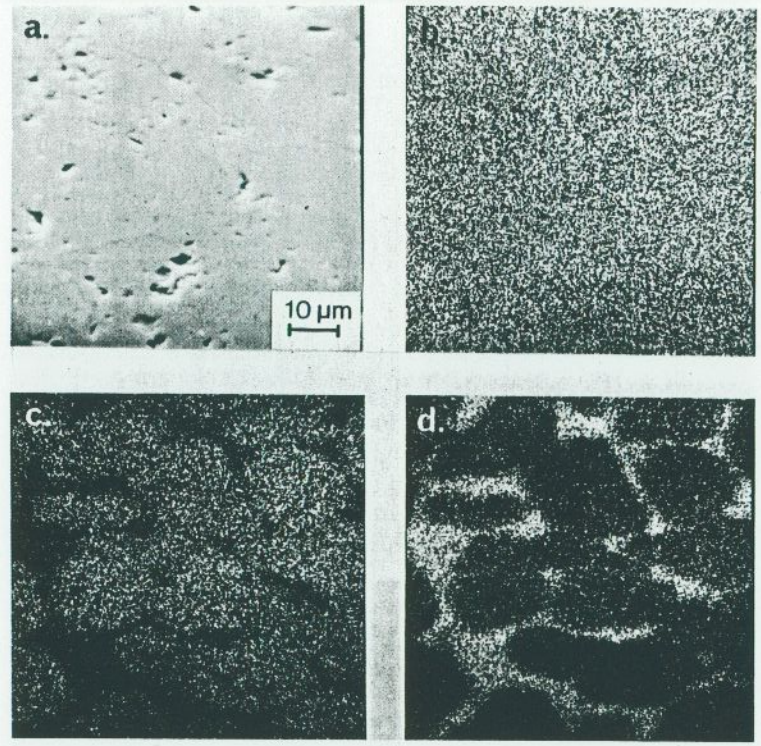

Fig. 4. A polished Portland cement clinker section as seen[129] by: (a) ordinary SEM (secondary electron) image; (b) a Ca–x-ray map; (c) a Si–x-ray map; and (d) an Fe–x-ray map. The scanning electron and Ca map do not give clear delineation of phases unlike the Si distributions within alite/belite phases and Fe concentration within the complementary interstitial matrix.

example, cement phase differentiation is difficult utilising the Ca x-ray maps alone, or distinguishing alites from belites from a Si x-ray map.

The use of chemical etching as a phase delineator has already been discussed in Section 2.2, although this is not favoured if microanalytical studies are to follow since reaction product deposition and leaching of the clinker all affect surface composition.[111] Ghose and co-workers[111,112] developed ion-beam etching as a phase-delineation aid for microanalysis work. The etching effects of an energetic argon ion beam (5 kV energy, 2 mA ion current operating at a pressure of 10^{-4} torr) onto resin-impregnated cut and polished (down to 0·25 μm diamond paste) cement

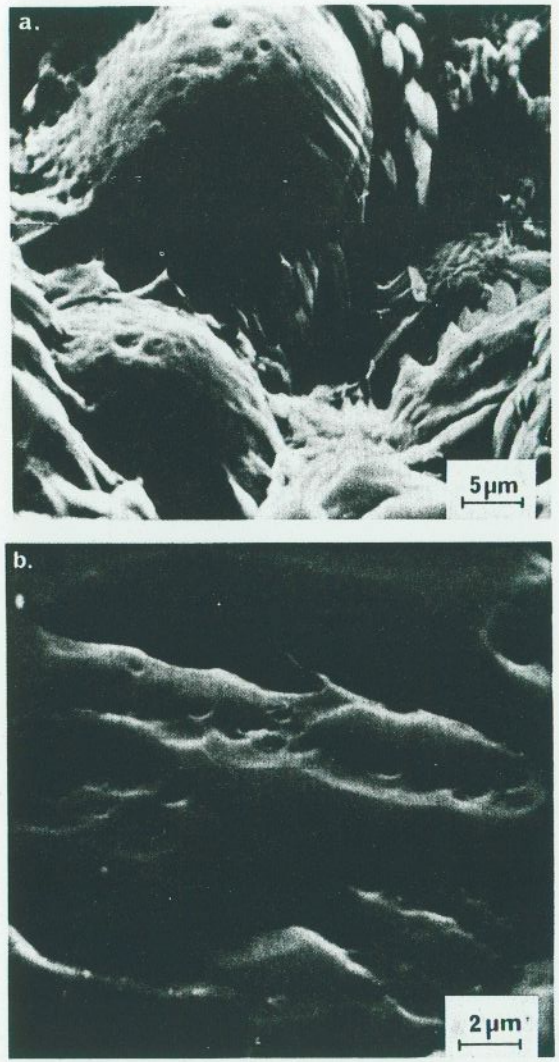

Fig. 5. SEM micrographs[129] showing the more extreme effects of ion-beam etching on polished clinker sections: (a) an etch-pit after 10 h of etching; and (b) a silicate grain differentiated but heavily damaged after 20 h of etching.

clinker sections were studied. The specimens were either kept stationary or rotated about an axis perpendicular to their plane. Different angles of incidence of the ion beam onto the specimen surface were used. For high–normal angles of incidence (70–90°), phase delineation was very poor and furthermore with the severe etch-pitting of the surfaces (Figs 5(a) and (b)) these conditions are most unsuitable for microanalysis. A low-angle etch (5–15°) for a short time (2–3 h) with continuous specimen rotation (depth of etch 0·2–0·3 μm) was found to produce optimum results (Fig. 6)—grain boundary delineation is good while the overall surface planarity is well maintained. Longer periods of etch with specimen rotation were found to introduce hummocky features onto the grain surfaces (Fig. 7). These hummocks were believed to nucleate around sub-surface defects or inclusions growing laterally with further etching; in the case of Fig. 7, the round hummocks on the pseudo-hexagonal alite grains are thought to have been nucleated by belite inclusions. These hummock features were found to be more numerous in the interstitial phase which is, of course, a generally less perfectly crystallised solid solution containing the occasional glassy phase. The silicates were found to be etched faster than the interstitial

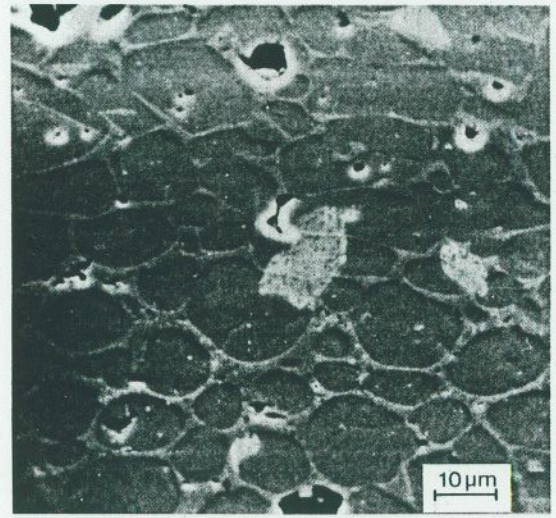

Fig. 6. SEM micrograph[111,129] illustrating the ideal grain boundary etching for phase delineation and subsequent microanalysis; the cement was etched at low angles of incidence for 3 h with continuous specimen rotation. Reproduced with the permission of Chapman and Hall Ltd, London.

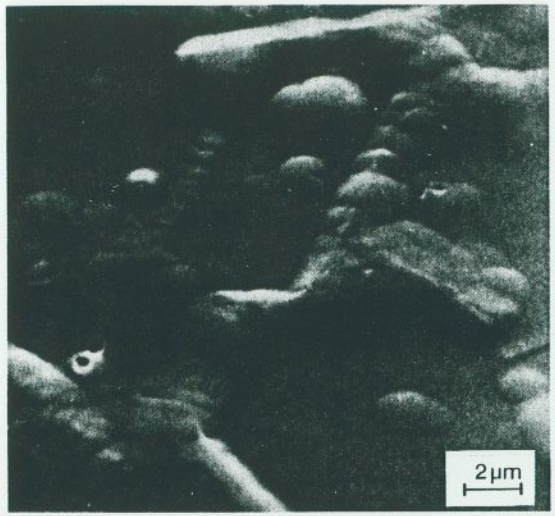

Fig. 7. SEM micrograph[129] showing the growth of surface hummocks in all clinker phases after prolonged periods (15 h) of ion-beam etching (with continuous specimen rotation and medium incidence angle of etch).

phase. The typical topography produced by medium (30–65°) angles of ion etching on stationary specimens is shown in Fig. 8.

Because of the ever-increasing use of the SEM–EDS method for quantitative analysis of cement systems, we shall discuss aspects of the experimental method in some detail before going on to discuss the results of different workers. If k is the ratio of the characteristic x-ray intensity I_B generated from element B in a specimen to that generated under identical electron–optical conditions from the pure element B (I_B^0) then the concentration, c, of the element B in the specimen is given by:

$$c = \frac{I_B}{I_B^0} k_Z k_A k_F = k k_Z k_A k_F \qquad (1)$$

This is the basis of the 'ZAF' correction method,[102,117,118] the individual corrections being: (1) the differences in electron scattering and retardation in the specimen and the standard, the *atomic number effect*, expressed by the factor k_Z; (2) *absorption* of the x-rays within the specimen, k_A; and (3) *secondary fluorescence* from both the continuum and characteristic x-rays generated, k_F. Midgley[119,120] and Fletcher[121,122] synthesised compounds

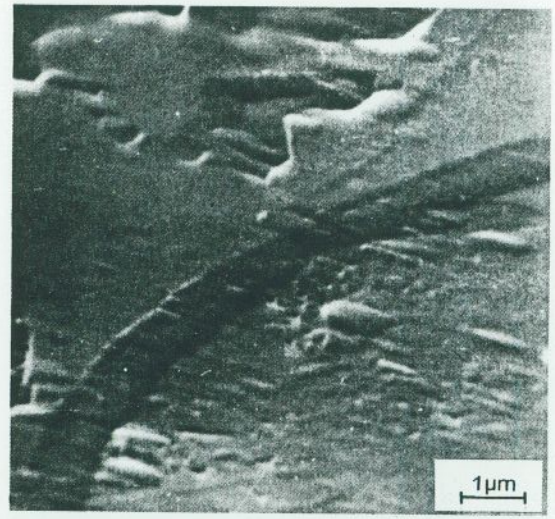

Fig. 8. SEM micrograph[112,129] showing directional etch on a stationary specimen after 11 h of etching at medium incidence angle.

of similar compositions to cement minerals for use as standards in their microprobe studies. To take into account all the major cement phases with their various solid solutions and numerous impurities would require an unrealistically large number of such compound standards but it has been shown by Blum *et al.*,[123] Russ[124] and Moore *et al.*[125] that the normalised x-ray intensities generated from pure elemental standards are constant for any given set of electron–optical and geometric conditions. Thus in practice, provided the variations in electron–optical conditions are not excessive, one need only standardise on a single pure element by utilising a previously determined calibration curve covering the required elemental range. This method, known as the 'single standard method', has been used by Barnes and co-workers[125–9,141,142] in the SEM–EDS analysis of cement clinkers. Silicon was chosen as the primary standard on account of its stability under both the electron beam and atmospheric exposure. Figure 9 depicts a standard calibration curve for a Cambridge Stereoscan II–EDAX 707B system obtained at an operating voltage of 22·8 kV, with 55° specimen tilt and a 45° x-ray take-off angle.[129]

The most accurate microanalysis requires that the specimen and standard(s) are coated (with electrically conducting layers) together so that the coating thickness is the same for both.

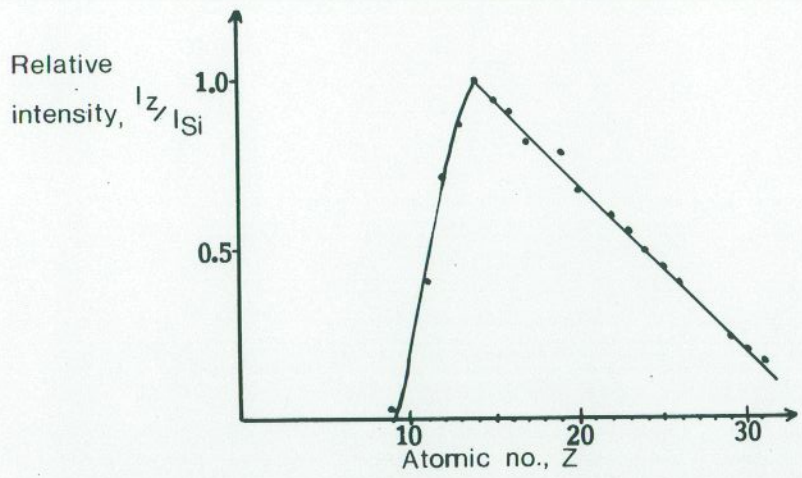

Fig. 9. Pure element standard calibration curve[129] obtained from a Cambridge SII SEM–EDAX 707B EDS operating at 22·8 keV, 55° specimen tilt, and a 45° x-ray take-off angle.

Carbon is preferred to any metallic coating because of its low atomic number, low linear absorption coefficient for x-rays, effective transparency to secondary electrons (at ~200 Å thickness), and low emission of white x-radiation. The accelerating voltage, specimen tilt and x-ray take-off angles are parameters which should be known accurately. An error of 1 kV in the accelerating voltage introduces an error of 1 % or more.[130] With a SEM–EDS system the accelerating voltage may be accurately (±50 eV) and readily obtained[131] from monitoring the x-radiation generated from a high atomic number specimen (e.g. molybdenum, $Z = 42$, $K_\alpha = 17{\cdot}4$ keV, $K_{absorption} = 20{\cdot}01$ keV) in the vicinity of the short wavelength cut-off. The specimen tilt and x-ray take-off angles should also be carefully computed from the system geometry. In most of the modern SEMs, microanalysis is performed with the specimen horizontal and x-ray take-off angles between 35 and 45° which are adequate. Even after taking all the precautions possible, systematic errors (particular to a given composite material) can arise. This is because the active EDS crystal area subtends a large solid angle at the specimen so that the true x-ray take-off angle varies around the calculated geometric value; there are also uncertainties regarding the precise corrections for x-ray absorption.[117] Ghose and Barnes[128] quantified and thereby removed these systematic errors for cementitious phases by performing careful

analyses of stoichiometric C_2S, C_3S, C_3A, C_4AF and C_6A_2F synthetic samples. Table 3 summarises the results and indicates the levels of correction required. The largest correction necessary was −2·7 wt % for calcium levels in C_3S phases. In applying these results to real cements, the C_2S/C_3S corrections were applied to belites/alites, respectively, and linear interpolations were applied between the $C_3A/C_4AF/C_6A_2F$ corrections (according to the F content) for the interstitial phases. No corrections were applied for the minor elements since, at concentration levels of 1 % or less, statistical errors predominate above any systematic deviations. Oxygen could not be detected in the system used for this analysis on account of the absorption of low-energy x-ray photons (all elements lighter than fluorine, i.e. $Z \leq 9$) by the Be window of the Si(Li) detector, and so oxygen content was (indirectly) calculated by difference. Kovacs and Tamas[117(b)] concluded that errors of several percent can result from inexplicit corrections for

TABLE 3

EVALUATION OF SYSTEMATIC DEVIATIONS[a] IN THE Ca, Si, Al AND Fe ANALYSIS FOR THE SEM–EDS GEOMETRY USED BY GHOSE AND BARNES[128,129]

Phase	*Element*	*Theoretical wt %*	*Experimental average wt %*	*Number of grains analysed (N)*	*σ*	*Random error* $\sigma/\sqrt{N}$	*Systematic deviation*
C_3S	Ca	52·66	55·35	115	0·72	0·07	+2·69
	Si	12·30	13·16		0·21	0·02	+0·86
C_2S	Ca	46·54	47·43	174	1·22	0·09	+0·89
	Si	16·31	16·99		0·37	0·03	+0·68
C_3A	Ca	44·50	45·88	20	0·39	0·09	+1·38
	Al	19·97	20·00		0·29	0·06	+0·03
C_4AF	Ca	32·99	34·89		0·89	0·14	+1·90
	Al	11·10	11·25	39	0·87	0·14	+0·15
	Fe	22·98	23·20		1·35	0·23	+0·22
C_6A_2F	Ca	34·35	36·23		0·76	0·12	+1·88
	Al	15·42	15·73	39	0·55	0·09	+0·31
	Fe	15·95	16·21		0·91	0·15	+0·26

[a] Systematic deviations are evaluated by statistical analysis of the experimental scatter obtained using known pure synthetic stoichiometric standards. It is seen that the metal concentrations are consistently over-estimated by the ZAF corrections in each case, the remaining oxygen weight (not given here) providing the balance to 100 %. The data in this table is reproduced with the permission of Pergamon Press Ltd, Oxford.

absorption by oxygen. However, this complication has been empirically removed here by adjusting the corrections for the differing oxygen concentrations of each main phase (Table 3). Diamond *et al.*[132,133] studied the applicability of SEM–EDS methods to rough fracture surface specimens of cement. They estimated the lateral spread of the x-ray generation volume to be about 1·5 μm. Variations in the take-off and electron beam-incidence angles pertinent to a fractured cement surface can cause significant variations in ratios of peak heights obtained from a given composition. However, by restricting the take-off angle to between 60 and 90° and the incidence angle to between 45 and 90°, more acceptable results were obtained. Even within these frameworks, microanalysis on a fracture surface is always suspect and is, at best, semi-quantitative.

Moore,[134] Peterson,[135] Midgley,[119,120,136] Yamaguchi and Takagi[38] and Fletcher[121,122] were amongst the first workers to use microprobe methods in the analysis of cement clinkers. Peterson[135] found potassium present in micropores as K_2SO_4 apart from its presence in belite and the interstitial phases. Midgley[119] in analysing alite in clinker found substitutions of Fe, Mg, Na, K, Mn and Al for Ca. Al and Ti substituted for Si while Al was found to occur in interstitial sites in the structure as well. Fletcher[121] analysed belites in clinker. His data suggested that K, Na and Mg mainly occupy Ca sites and that Fe, Al, Ti and Mn occupy Si sites. The Al:Fe ratio in the belite grains corresponded well to the ratio of Al:Fe in the cement clinker, and this was found, by Midgley,[120] to hold for alite grains as well. In studying the partitioning of minor elements between co-existing alite and belite grains, Midgley[120] found considerable inhomogeneity in the sample populations and concluded that this stemmed from gross inhomogeneities within the initial raw material and that the mainly solid-state reactions in the kiln were not sufficiently energetic nor did they continue for long enough to average out these differences. Fletcher[122] analysed the interstitial aluminate and ferrite phases in clinkers. Where the aluminate and ferrite could be differentiated, Ti and Mn were found mainly in the ferrite phase and K in the aluminate phase. Sometimes, K_2SO_4 was found as a separate phase. He found 4·6 % Fe_2O_3 and 2·1 % SiO_2 present in C_3A in solid solution; 2–3 % SiO_2 was found in solid solution in the ferrite phase as well. Midgley and Bennett[137] have shown, from microanalysis, that larnite and bredigite co-exist in mineral samples from Scawt Hill (near Larne, Northern Ireland). The larnite was therefore not formed by polymorphic inversion from the higher-temperature-stable form, bredigite. Regourd and Guinier[138] found trigonal alite to contain less MgO but more Al_2O_3 and SO_3 than the monoclinic form. They also noted that the

solubility limit of certain ions such as Al, Fe, Na and K in belite decreases from the α to the α' then the β phases, which results in the exsolution of such ions along the lamellae of α' and β belites rendering quantitative microanalysis difficult in such cases. Hornain[139] studied the ferrite phase in clinkers by microanalysis and concluded that it was often close to brownmillerite (C_4AF) if substitutions due to SiO_2, MgO, TiO_2 and Mn_2O_3 are taken into account. Intergrowth of crystals of C_3A and C_4AF with very fine grains of belite often makes microanalysis difficult.

Kristmann[140] and Ghose, Barnes and co-workers[126–9,141,142] have reported on microanalysis of cement clinkers. Ghose and Barnes[128,129,141] investigated lattice substitutions and preferential incorporation of the minor elements into the silicates and the interstitial phases. They observed Na, Mg, Al, P, S, K and Fe to be present in the silicates nearly always in measurable quantities with Ti, V, Cr and Mn occasionally present. A computer fitting was made to the alite/belite analyses, comparing the fits obtained using various substitution schemes with the stoichiometric value. The general substitution scheme of Na, Mg and K substituting for Ca and Al, P, S and Fe substituting for Si, consistent with crystal chemical rules regarding ionic radii and charge, was found to be generally valid. Sometimes interstitial site occupancy also took place to minimise the charge imbalance of the oxygen network. Occasionally, especially with Al in alites, better fits were obtained by dividing the Al content between the Ca and Si sites, in keeping with the known ability of Al to exist in both four- and six-coordination with oxygen[143] and thus be capable of substituting for both Ca and Si. For the interstitial matrix, 2–3 % Si was consistently found to be present (in keeping with Fletcher's[122] finding) preferentially substituting for Al. Ti and Mn were found to be generally confined to the interstitial phase substituting for Fe, with P and S substituting for Al. In white cements, the interstitial matrix is C_3A while in sulphate-resisting clinkers, the compositions were found to be in the 'C_6A_2F–C_6AF_2' alumino-ferrite range. In ordinary Portland cements, however, there appeared to be a further solid solution between C_3A and the alumino-ferrites. Evidence for this was also noted by Kristmann[140] in cement clinkers and he proposed the compositional formula $Ca_3(Fe_{1-p}Al_p)_2O_6$ ($0{\cdot}80 < p < 0{\cdot}90$) for this solid solution. Tarte[144] has also achieved such a solid solution in a synthetic mixture of C_3A and C_4AF.

Ghose and Barnes[141] also studied the partitioning of the minor elements amongst the cement clinker phases while comparing the 'microscopic' values obtained from SEM–EDS analysis with the overall or 'macroscopic' compositions of the clinkers as determined from bulk wet chemical

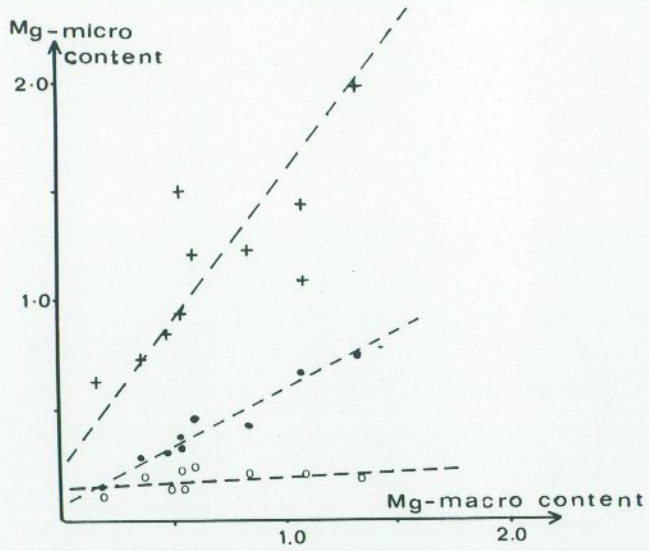

Fig. 10. Variation[129,141] of average *micro*-Mg content within each phase type versus the *bulk* clinker Mg content. The relationship is linear with the interstitial (+) and alite (●) phases, while the belite (○) phase appears to exhibit an upper micro-limit of 0·2% Mg.

analyses. Figure 10 illustrates the results for Mg. It is seen that the average Mg content of alite and interstitial phases increases approximately linearly with that of the bulk clinker, whereas with belites the Mg content reaches a microscopic upper limit of 0·2% this being lower than the accepted solubility limit of 0·3–0·6%. The interstitial matrix is thus seen from Fig. 10 to be the major sink (apart from periclase inclusions) for Mg in clinker. The higher levels of Mg in alites compared to belites are also in keeping with the supposed stabilising effect of Mg on alite.[145] The average belite S content increases approximately linearly (Fig. 11) with the bulk clinker S content, while for alites it is always close to 0·05–0·10% which corresponds to the solubility limit of sulphur in alite above which dissociation into belite and CaO occurs.[145] Sulphur content in the interstitial matrix is generally low, although individual K_2SO_4 and Na_2SO_4 crystals are sometimes found embedded in the matrix. The potassium content of belites in clinkers manufactured by the wet process is found to be generally higher than in those by the dry process (Fig. 12). No clear correlation is evident with the interstitial phase while for alite the average level was below 0·1%, in

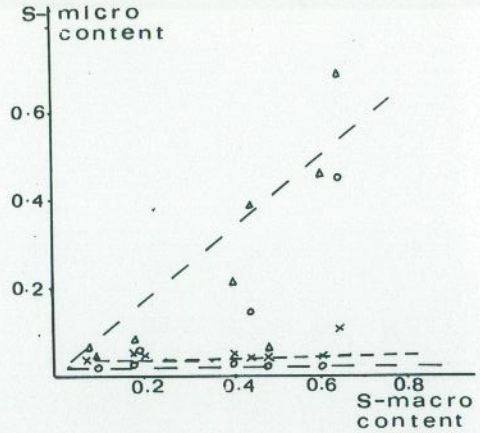

Fig. 11. Variation[129,141] of average *micro*-S content within each phase type (×, alite; △, belite; ○, interstitial) versus the *bulk* clinker S content. Only the belite phase appears to exhibit a linear relationship.

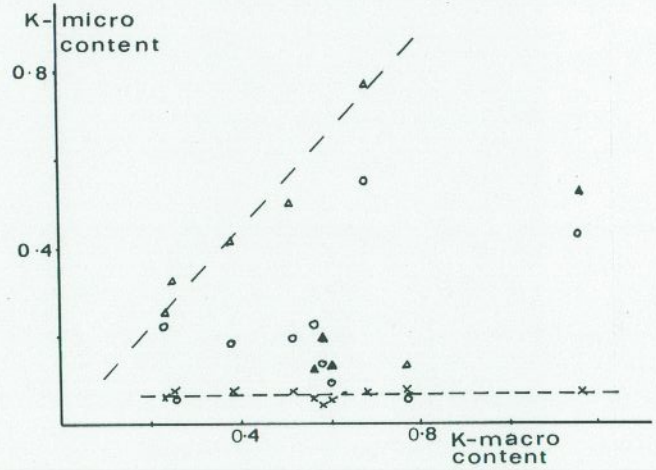

Fig. 12. Variation[129,141] of average *micro*-K content within each phase type (indicated) versus the *bulk* clinker K content. The belite phase (wet process) (△) shows a linear relationship, while the alite (×) phase exhibits an upper limit of 0·1. The belite (dry process) (▲) and interstitial (○) phases do not appear to exhibit upper limits, although the relationships are not obviously linear.

keeping with the idea of K being an effective disrupter of alite.[145] The average Fe contents in alite and belite increase nearly linearly with the bulk Fe content—the full results are published elsewhere[129,140,141] although it can be reported that no trend of preferential incorporation is evident. The Al:Fe ratio in both silicate phases is also found[120,129,141] to increase linearly with the overall Al:Fe ratio of the bulk clinker. Phosphorus is found to be more abundant in both silicate phases, and sodium is more abundant in the interstitial matrix than in belites while for potassium the reverse is true. Kristmann[140] observed, on the basis of greater alkali incorporation into belite, that it is the last phase type to crystallise in the kiln. Lehmann *et al.*[146] argued that the interstitial phases crystallise last on the basis of their higher alkali content. Since the behaviour of sodium and potassium proved to be quite the opposite in their study, Ghose and Barnes[141] felt that predictions based on ionic mobility alone may be misleading. In Kristmann's[140] study, S, Na, K and Fe were found mainly in belite and Mg in alite, while Al occurred in both. However, wet process clinkers tend to contain Al preferentially in alite, while dry process clinkers usually contain Al preferentially in belite.

In another study, Ghose and Barnes[142] noticed a concentration of lath and rounded structures around a vesicle region in a wet process cement clinker (Fig. 13). Microanalysis suggested that these structures are high-potassium substituted forms of belite, the potassium content varying between as much as 9·5 and 24 % by weight. The atomic compositions of the two most extreme samples were:

$$(Ca_{1\cdot33}Na_{0\cdot13}Mg_{0\cdot01}K_{0\cdot41}Al_{0\cdot07})\cdot(Si_{1\cdot05}P_{0\cdot01})O_{3\cdot99}$$

and $$(Ca_{0\cdot54}Na_{0\cdot04}Mg_{0\cdot25}K_{1\cdot06}Al_{0\cdot29}Fe_{0\cdot06})\cdot(Si_{1\cdot03}Al_{0\cdot20})O_{3\cdot54}$$

The oxygen concentration was determined indirectly by difference and is hence liable to larger errors. These K concentrations are much higher than in $KC_{23}S_{12}$, the K-stabilised α-'C_2S noticed previously in clinkers. Midgley[120] found that belites are sometimes found concentrated around vesicles in the clinker, which may have contained gaseous potassium ions since flue gases are often rich in potassium. One might conjecture that, under such conditions, potassium might conceivably be incorporated into the belite lattice above its solubility limit with heavily defective but, nonethlesss, stable belite-like structures.

3.3. Transmission Electron Microscopy (TEM) and Microanalysis (MA)

Although TEM studies have long been used for morphological studies on unhydrated and hydrated Portland cements (see also comments in Section

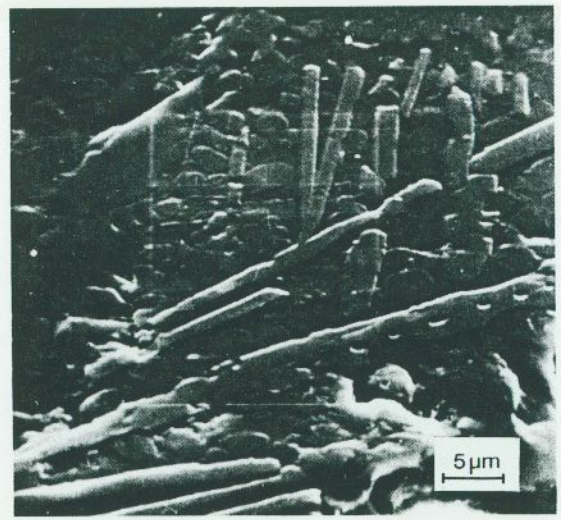

Fig. 13. SEM micrograph[129,142] of an area of lath and rounded high-K belite structures found around a vesicle region of a clinker.

3.4), the quality of cement electron microscopy has advanced in the last decade or so chiefly through overcoming the electron-penetration problem. For example, Hale and Henderson Brown[147] have shown that electron penetration through cementitious specimens is typically half that of ceramics such as glass, or metals such as iron, so one must use specimens of thickness down to 0·7 μm for sufficient electron transparency to obtain acceptable (contrast and resolution) electron micrographs at operating voltages of 100 keV; at voltages of 1000 keV, the acceptable thickness increases to about 4 μm. In addition to high-voltage microscopy, new thinning techniques, such as ion-beam thinning, have also contributed to overcoming the electron-penetration problem by providing a more acceptable (i.e. less mechanical damage and better consistency than with mechanical and chemical methods) way of thinning to sub-micron thickness than previously afforded by the techniques of grinding, microtomy and extraction. In this section the recent advances brought about by high-voltage electron microscopy and ion-beam thinning are considered in more detail.

The problems of preparing electron-transparent specimens have been avoided by a number of workers using the classical preparation by surface replication. Boikova *et al.*[148] used celluloid carbon replicas in their studies

of the defect state of C_3P-doped belites using HNO_3–alcohol etch. The etch pit density was found to reach a maximum at about 6 % C_3P, stabilising the most hydraulically active β-form. Further phosphate addition reduced both the hydraulic activity and the density of etch pits and converted the belite into the α'- and finally the α-form. The etch pits were found to be linearly arranged in β-C_2S but randomly in α'- and α-C_2S. Carbon replicas were also used by Papiashvili *et al.*[149] to study the distribution pattern of cracks and fractures on the surfaces of C_2S and C_3S grains after grinding. Mosaic, dendritic, lamellar and other types of fracture pattern were observed, the dislocation density reaching 10^8–10^9/cm^2. Vasileva *et al.*[150] heated β-C_2S at 1100 °C for 1–10 h, examining the dislocation structure using replicas, and found it to be essentially unchanged during this time-span. In a related study,[151] they prepared belite clinkers from pure oxides and cooled them from the sintering temperature (1420 °C) under different conditions. Clinkers cooled first without isothermal holding exhibited rounded, oval and dense forms of belite. In clinkers cooled with isothermal holding for 1 h, the belites exhibited short intersecting dislocation lines, arising out of the rearrangement of the crystal lattice due to plastic deformation. Deloye and Louarn[98] used extraction replicas to study the minor components found mainly at the interface between the belite and aluminate phases in clinkers. Some of the phases identified by micro-diffraction were C_2F, C_3S_2, NC_8A_3 and $KC_{23}S_{12}$. The use of ion-beam thinning for cement clinkers was first reported by Yamaguchi and Takagi[103] who reported on the observation of dislocation loops, stacking faults, and bend and strain contours in alite and inversion twinning in belite. Ion-beam thinning has recently been used to prepare TEM specimens by Ghose and Barnes[40] and Groves and Hudson.[41] Before thinning in the ion-beam, it is necessary to prepare optical thin sections (20–30 μm thick) using standard metallographic methods (see Section 2). During the final ion-thinning stage, the silicate phases sputter faster than the interstitial phases and hence, to minimise differential thinning, the 'self-shadowing' principle must be utilised[111] by inclining the ion beams to glancing angles of incidence (5–15°) to the specimen. Acceptable thinning parameters are 5–6 keV argon ions at 1–2 mA beam currents and 10^{-4} torr pressure and 1 μm/h/gun would be the usual rate of sputter for cementitious materials with thinning from both sides using two guns. Irregular specimen puncturing can be a problem, especially with porous material, and argon implantation is fairly common.[152] As the thinness of the specimen around the puncture site is often uneven, it is advantageous to use a high-voltage electron microscope (HVTEM) if such access can be gained. Thus it has

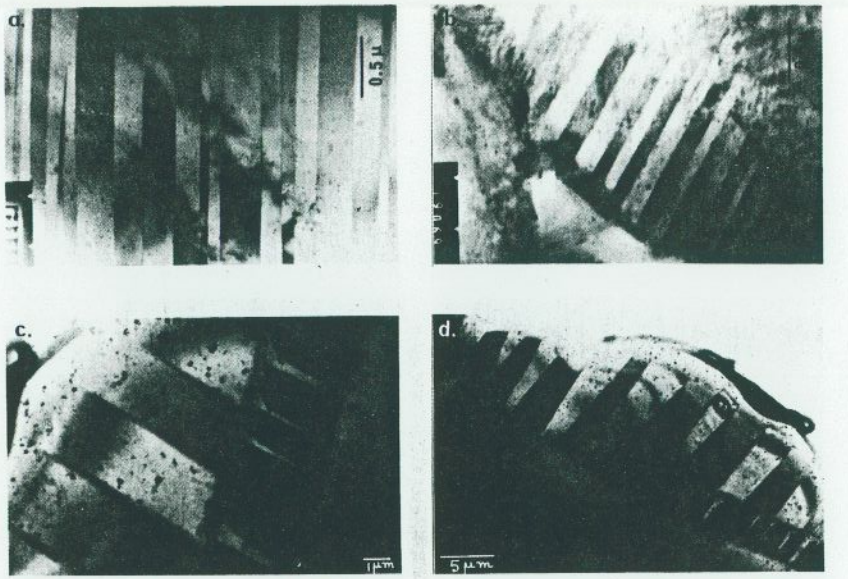

Fig. 14. TEM micrographs[40,129,152] of belite striations in ion-beam thinned cement clinker. The width of striations varies between < 1 000 Å and 5 μm: (c) and (d) show two co-existing parallel sets of striations, one set being five- to six-times narrower although without any apparent exact numerical register. The reciprocal lattice sections are probably perpendicular to [1$\bar{3}$1] ((b)), and [010] ((c) and (d)). ((a) and (b) reproduced with the permission of World Cement, Surrey.)

now become possible to directly image the narrow lamellae (0·1–0·3 μm widths) of the cement belite phase; Fig. 14 shows examples of these in different orientations. Figures 14–16 and 21(c) (later) also give indications of a yet finer substructure sometimes with clear signs of internal twinning (e.g. Fig. 15) within each lamella. Most often the lamellae are [100] reflection twins[39,41,152] as deduced from the electron-diffraction patterns—these and other implications are discussed in Section 3.4.

In a recent study at the University of Illinois at Urbana[152–4] TEM methods have been used in characterising Ba-, P- and B-stabilised β- and α'-C_2S. Ion thinning was used for specimen preparation. Figure 16 shows three adjacent P-stabilised β-C_2S grains with an amorphous grain boundary phase. The β-C_2S grains show twin lamellae and indications of some α or α–δ fringes[155] at some of the twin interfaces. The grain boundary region contains Ca and Si with widely varying ratios (Ca:Si between 1·1 and 2·8), indicating gross inhomogeneity in this amorphous phase. Figure 17

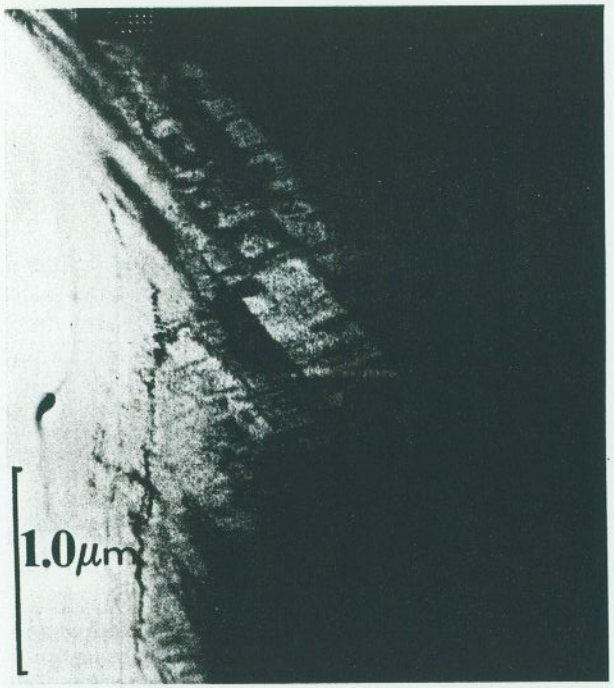

Fig. 15. TEM micrograph[152] of a P-stabilised β-C_2S specimen (ion-beam thinned) showing finer striations (widths of the order of a few hundred ångstroms) within individual twin lamellae.

shows linear arrays of precipitates in a B_2O_3-stabilised α'-C_2S grain along alternate dark bands. The composition and crystallinity of these precipitates are uncertain at the present time; although it appears that they form along preferred crystal planes of the host lattice, it has not yet been possible to index the planes and further work is required for a full clarification. Figure 18 is of a BaO-stabilised α'-C_2S crystal—linear arrays of precipitates and dislocation tangles are evident along the alternate dark bands. The two sets of such alternate bands meeting at an angle are suggestive of adjacent grains, although no clear grain boundary is visible.

TEM microanalysis has gained momentum in cement studies in recent years. Taylor's group has published TEM–EDS analyses of cement hydration products.[156,157] The main advantage of TEM–EDS analysis over the microprobe method is the greatly improved spatial resolution of the order of hundreds of ångstroms obtained with thin electron transparent

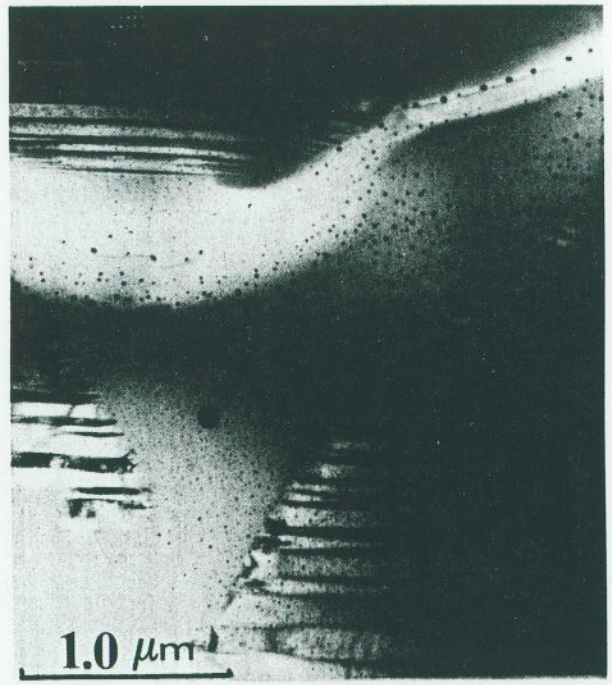

Fig. 16. TEM micrograph[152] of a P-stabilised β-C_2S specimen (ion-beam thinned) showing a triple-grain boundary phase.

specimens. Generation of spurious x-rays from sources other than the specimen itself is, however, much more pronounced in the TEM (because of the small specimen chamber) than in the SEM. The principal sources of extraneous x-rays are the specimen rod, the specimen grid, the anticontaminator and the electron–optical column itself, but for cement studies these are unimportant. Methods of quantitative analysis have to be modified for thin-section microanalysis since the x-ray intensity generated varies with specimen thickness which is difficult to measure. It has, however, been demonstrated[158–60] that reliable quantitative information can be obtained using the somewhat simpler 'ratio technique'. The application of this method is dependent on the 'thin film criterion'—this requires that the specimen, in addition to possessing observable contrast under the acceleration voltage used, should be thin enough so that x-ray absorption and secondary fluorescence are sufficiently small to be

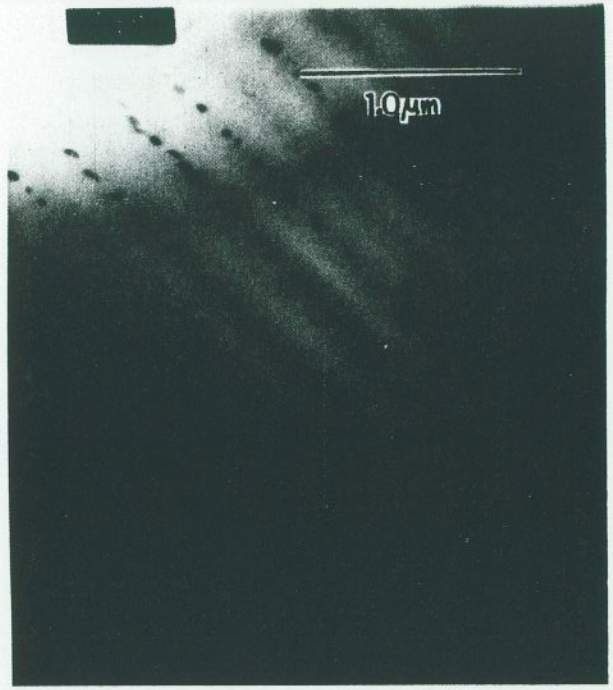

Fig. 17. TEM micrograph[154] of a B-stabilised α'-C_2S specimen showing linear arrays of precipitates.

neglected. In practice, this would correspond to specimen thicknesses of under 1000 Å. In such a case, the ratio of two characteristic x-ray intensities I_A/I_B produced from a specimen containing atoms of elements A and B, respectively, is directly proportional to their weight fractions (C_A and C_B):

$$\frac{C_A}{C_B} = k\frac{I_A}{I_B} \tag{2}$$

In terms of atomic ratios, this becomes:

$$\text{Atomic Ratio}\frac{A}{B} = k\frac{\text{Atomic weight B}}{\text{Atomic weight A}}\frac{I_A}{I_B} = k\frac{I_A}{I_B} \tag{3}$$

The proportionality constant, k, is an instrumental constant for a given accelerating voltage and thus effectively embraces the differences in efficiencies of x-ray generation from different elements and the attenuation

Fig. 18. TEM micrograph[154] of a Ba-stabilised α'-C_2S grain showing precipitates in two sets of bands meeting at an angle of about 45°.

of x-rays through the Be window of the Si(Li) detector. In practice, k can be determined for different pairs (A and B) of elements from the analysis of suitable standard specimens. Ghose and Barnes[129,161] analysed belites in a cement clinker using the ratio technique and compared the results (from the same clinker) with those of the SEM–EDS method. Table 4 summarises the results from these analyses. For many of the belites, and even for synthetic stoichiometric C_2S crystals, the Ca:Si atomic ratio is seen to be less than 2 with TEM analysis whereas this was never the case for SEM determinations; similar results were also obtained for synthetic C_3S samples. Apart from the major constituents, the TEM generally appeared to present a picture of greater incorporation of minor elements into belites than would be gained from SEM analyses. This might, in principle, be attributable to the difference in experimental and data-handling procedures and wider sampling in the TEM study. However, loss of certain

TABLE 4

RESULTS OF MICROANALYSIS ON BELITES, COMPARING THE VALUES[a] OBTAINED FROM TEM ('RATIO TECHNIQUE) AND SEM (FULL ZAF CORRECTION).[129,161] THE Ca:Si RATIO IS CONSISTENTLY LOWER BY TEM EVALUATION, WHILE TEM APPEARS GENERALLY TO OVER-ESTIMATE THE MINOR COMPONENTS. (POSSIBLE REASONS FOR THIS ARE DISCUSSED IN THE TEXT.)

Method of analysis		*Ca*	*Si*	*Na*	*Mg*	*Al*	*P*	*S*	*K*	*Fe*
TEM–EDS: beam voltage = 80 keV; take-off angle = 50°; specimen tilt = 0° (to horizontal); number of grains = 25	Spread:	1·61–2·33	1	0–0·06	0–0·09	0·03–0·25	0–0·02	0–0·05	0–0·07	0·01–0·08
	Mean:	2·00		0·02	0·05	0·06	0·005	0·02	0·02	0·03
	Standard deviation:	0·18		0·02	0·02	0·04	0·004	0·01	0·02	0·01
SEM–EDS: beam voltage = 22·8 keV; take-off angle = 45°; specimen tilt = 55° (to horizontal); number of grains = 9	Spread:	2·13–2·39	1	0·01–0·03	Tr–0·02[b]	0·05–0·10	Tr–0·02[b]	Tr–0·03[b]	Tr–0·01[b]	Tr–0·02[b]
	Mean:	2·29		0·016	0·013	0·08	0·011	0·013	0·006	0·013
	Standard deviation:	0·08		0·006	0·005	0·02	0·004	0·008	0·003	0·005

[a] All values are expressed as atomic ratios relative to Si.

[b] Tr denotes trace amounts below 0·01.

elements under the focussed TEM probe was clearly evident in some cases. For example, with pure NaCl grains, the Na:Cl peak height ratio decreased rapidly with time indicating loss of Na under the probe. It is also interesting that TEM analysis failed to detect Na in most belite grains. Some of the α-CS (pseudo-wollastonite) grains, used in the calibration procedure, indicated Ca loss under similar conditions. Such losses are easily confirmed from the progressive degradation of the electron diffraction patterns. There are other reports of Mg and K losses in geological samples under the TEM probe.[158] This problem is not usually encountered in SEM or probe microanalysis, where lower probe voltages and larger specimens reduce the effects of electron-beam damage and heating. The problem can be minimised by using the low-dose beam currents that are compatible with a reasonable x-ray count rate. Ghose and Barnes[129,161] tested the ratio technique by calculating k-values over several stoichiometric compounds; the results obtained from two TEMs under differing electron–optical conditions are very similar (Fig. 19), thus indicating the wider validity of the 'thin-film criterion'.

3.4. TEM–Electron Diffraction (ED)

For further details concerning the methodology of TEM–electron diffraction, the reader is referred to the literature;[91–102] the texts by Gard[96,97] discuss electron diffraction from several cementitious materials and techniques of crystal axis alignment. Although ED has long been used as a means by which particular cement phases can be identified or confirmed from their known crystal lattice parameters, the advent of techniques described in Section 3.3 allow one to more effectively combine the detailed microstructural observations with diffraction and thus gain further clues to the origin of different cement phases.

The TEM–ED of cement belites is considered first since reference has already been made to these studies. The topic of special interest is that of the fine β-C_2S parallel lamellae which suggest polysynthetic twinning, since electron optics alone have been able to resolve this issue unambiguously. TEM–ED observation on these fine lamellae has been reported from at least three sources: Jelenic *et al.*;[39] Ghose and Barnes;[40] and Groves.[41] The most commonly reported reciprocal lattice sections are [010] (i.e. [010] planes perpendicular to the incident electron beam), although, additionally, Groves[41] has reported [100] and [0$\bar{1}$2] sections, and Ghose and Barnes[40] have reported another section, probably [1$\bar{3}$1]. Various sections and forms of possible β-C_2S polysynthetic twinning are illustrated in the TEM micrographs of Figs 14, 15, 20(d) and 21.

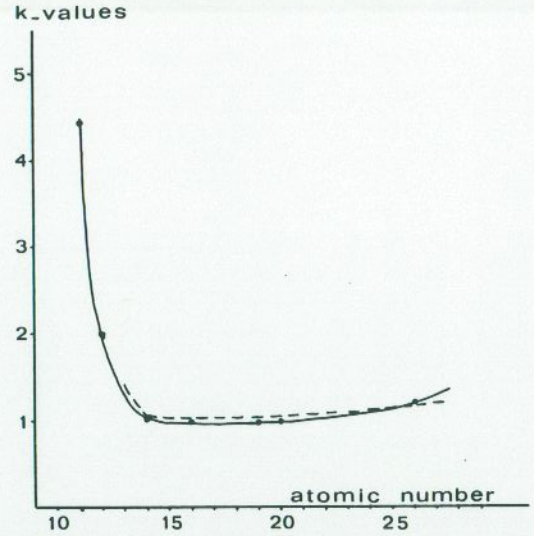

Fig. 19. TEM–EDS (energy dispersive system) 'k-ratios' measured[129,161] for various atomic numbers and obtained under different electron–optical conditions. The solid curve was obtained from an AEI CORA 2 microscope, and the dashed curve was from a JEOL TEMSCAN 120CX instrument calibration. For CORA details see Table 4 (TEM); the TEMSCAN electron-optical conditions are 100 kV, 45°/45° tilt/take-off angles.

The polysynthetic twinning across [100] reflection planes should yield an (h0l) diffraction pattern such as that indicated schematically in Fig. 20(b), which can be simply envisaged as the superposition of two reciprocal lattice sections corresponding to one β-C_2S and its reflection twin. Since the monoclinic β-angle (or equivalent reciprocal lattice β^*-angle) for C_2S is close but not equal to 90°, the result is a splitting of all (h0l) reflections when $l \neq 0$ as illustrated. This is precisely the kind of (h0l) pattern observed by both us and Groves, an actual example being given in Fig. 20(d). Furthermore, the angle $\Delta\theta$ between the two twin a (or a^*) directions has been measured (from Fig. 20(d)) as $9{\cdot}05 \pm 0{\cdot}05°$.

Since from Figs 20(a) and (b):

$$\Delta\theta = 180 - \beta^* - \beta^*$$

and for a monoclinic unit cell:

$$\beta^* = 180 - \beta$$

then

$$\beta = (\Delta\theta + 180)/2 = (9{\cdot}05 + 180)/2 = 94{\cdot}53°$$

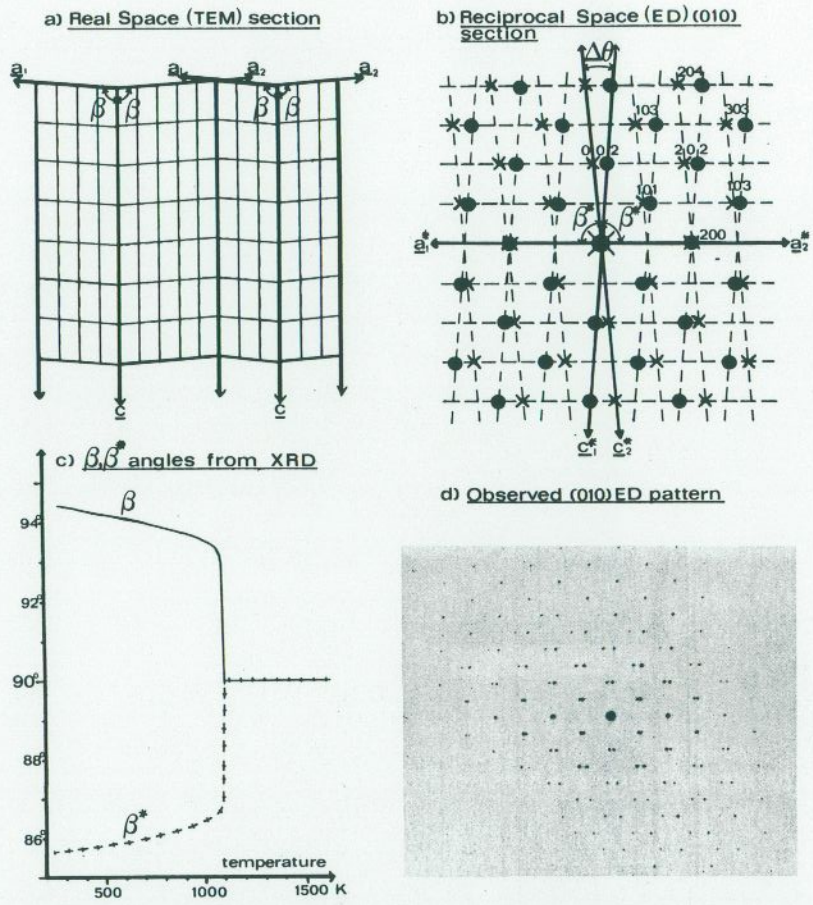

Fig. 20. Explanation for the splitting of diffraction spots with β-C_2S polysynthetic twinning as observed in the (010) section: (a) and (b) illustrate the twinning in real and reciprocal space, respectively, of which the latter may be directly compared with the observed diffraction pattern in (d).[152] The crystallographic β-angle of 94·53° measured from (d) compares well with the refined value, 94·34°, obtained by Barnes *et al.*[28] from the extrapolated accurate high-temperature x-ray data in (c).

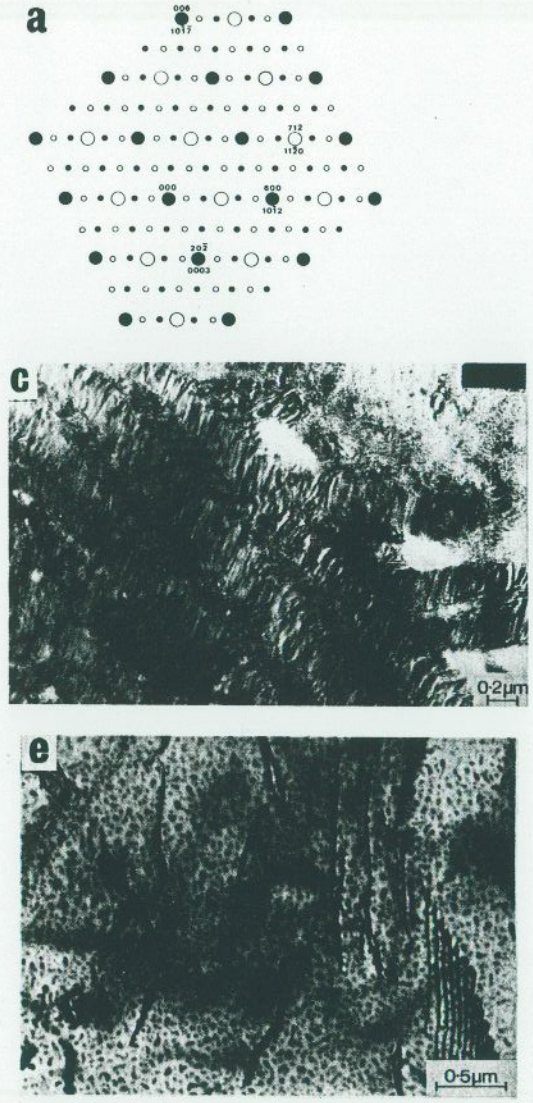

Fig. 21. TEM–ED observations on Portland cement clinker by Groves.[41] (a) illustrates the relationship between the pseudo-hexagonal (larger circles, hexagonal indices) and true monoclinic (smaller circles) reciprocal lattices for alite—closed circles correspond to zero layer (h0l), and open circles to first layer points; (b) actual diffraction pattern obtained in same section as (a); (c) internally twinned belite

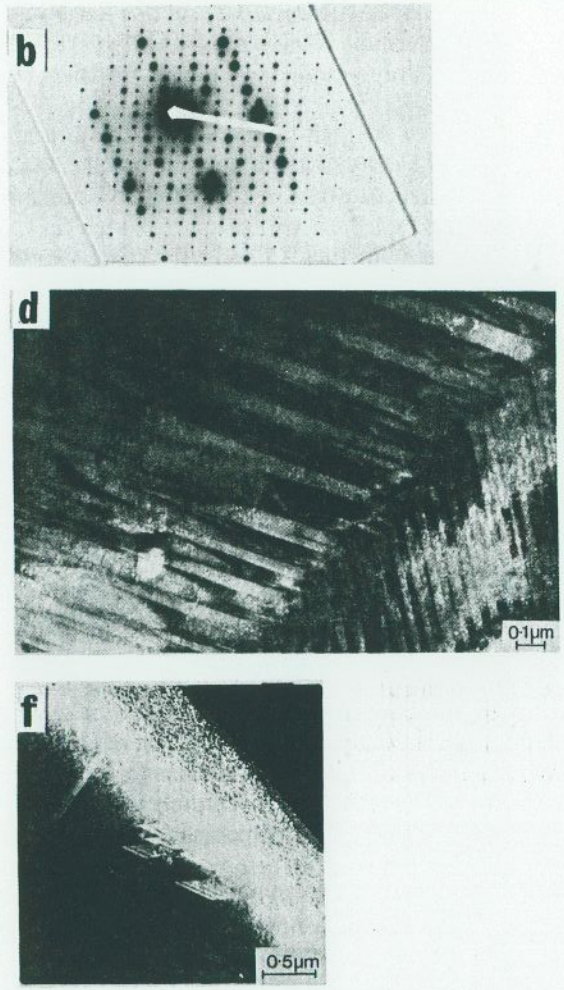

Fig. 21.—*contd.*
(probably β-C_2S, electron beam parallel to [100]) showing finer substructure indicative of a martensitic transformation; (d) two sets of twin bands in β-C_2S related by 120° rotation, indicative of a parent hexagonal α-C_2S phase; (e) and (f) defect structures in C_3A—(e) dislocation arrays in Buxton alite, (f) planar defects, [$\bar{2}$205] dark field. (Reproduced by permission of Pergamon Press Ltd, Oxford for (a), (b) and (f), and Chapman and Hall Ltd, London for (c), (d) and (e). Prints by courtesy of Dr G. W. Groves, University of Oxford.)

This value is in fair agreement with the more accurate XRD-refined value of 94·34° (see Fig. 20(c)) determined by Barnes *et al.*[28] for synthetic pure C_2S. The case then for β-C_2S polysynthetic twinning across the [100] reflection plane seems definitive.

Two other vital clues to the high-temperature formation of β-C_2S have been noted by Groves.[41] Firstly, that within each lamella twin can often be seen some common substructure (referred to as 'substriations' or 'internally twinned structure'), examples of which can be seen in the work of Ghose[152] and of Groves[41] in Figs 15 and 21. Where two different and apparently unrelated sets of lamellae intersect, the substriations within each set sometimes appear as common (parallel) to both sets. This formation can be explained in terms of a martensitic transformation* in which a common slip of an earlier higher (i.e. α- or α'-C_2S) phase is accommodated on inversion to the β-phase by two quite different sets of lamellae twinning. Secondly, Groves[41] finds an example of two sets of lamellae (reflection twins) offset by 120°. This is strongly suggestive of an earlier common α-C_2S region from which, on cooling, two out of three mirror planes (at 120°) of the α-hexagonal lattice have acted as two sets of shear planes for alternate twinning in order to neutralise any lattice strain incumbent on the $\alpha \rightarrow \beta$ inversion.

Groves[41(c)] has further been able to subdivide the β-C_2S twinning structure, as to whether it has been formed from α- or α'-C_2S. Two types of twin structure are identified:

1. $\alpha' \rightarrow \beta$: *optically resolvable twins* on single set of [100] planes formed by shear distortion of unit-cell parameters ($c_{\alpha'} \rightarrow b_\beta$, α'-90° unit-cell angle $\rightarrow \beta$-94·34° if we take the accurately x-ray-determined value of Barnes *et al.*[28] from high-temperature studies as shown in Fig. 20(d)).
2. $\overrightarrow{\alpha \rightarrow \alpha' \rightarrow \beta}$: *TEM-resolvable* [*100*] *twins* ($\sim$2000 Å width) with three orientations possible (choice of three equivalent shear planes with common [001] from the original α-phase) within the twin domain structure.

This analysis by Groves[41(c)] shows that one could, in principle, distinguish from the twin structure observed by thin-specimen TEM whether or not the $\alpha \rightarrow \alpha'$ transition temperature (1420°C) has been achieved locally in the kiln. The observation cannot, however, distinguish between $\alpha \rightarrow \beta$ and $\alpha \rightarrow \alpha' \rightarrow \beta$ inversion routes, although the former is generally considered more probable.

* A 'martensitic transformation' is a solid-state structural transformation, normally isothermal, arising through cooperative small displacements of large numbers of atoms such that a definite orientational relationship exists between the parent and the new phase. The effective driving force may be mechanical (e.g. shear stress), and the associated volume change is usually small.

More recent microstructural (precipitation) observations of these lamellae are given in Section 3.3 (Figs 16–18).

Regarding recent TEM–ED of cement alites and C_3A, the major work is that of Hudson and Groves.[41(a)] They found that the predominant structure of clinker alites is the monoclinic structure determined by Jeffery[35] for $C_{54}S_{16}AM$. They further point to the apparent similarity (i.e. pseudo-symmetry) of this low-temperature monoclinic form to the higher-temperature trigonal structure. This similarity is sufficient to accommodate the true $\{21\bar{1}0\}$ mirror planes of the trigonal lattice becoming identifiable pseudo-mirror planes (i.e. (712) or $(7\bar{1}2)$) in the monoclinic form. A plausible reasoning is that, on cooling, a transformation from trigonal $\rightarrow$ monoclinic occurs in which different regions of the trigonal phase will choose differently one of three $\langle 11\bar{2}0 \rangle$ directions to become the new monoclinic *b*-axes. The relationship between these regions might be described as 'pseudo-twinning' and Groves and Hudson[41(a)] present evidence to support this, including a consequent explanation for some of the weak XRD reflections which were unexplained[35] on the Jeffery lattice alone. Since this publication, Jeffery[162] has checked the effect of such pseudo-twinning across $\{21\bar{1}0\}$ on the interpretation of his original x-ray data (Laué, rotation and Weissenberg photographs) for the synthetic $C_{54}S_{16}AM$ alite, and agrees that all his observations of extra reflections can now be explained by micro-twinning without the need for any postulation of a larger unit cell for alite.

Hudson and Groves[41(a)] have also found a different alite lattice at higher temperatures from an *in situ* heating (700 ± 100°C) HVTEM experiment in which the clinker lattice transformed into a similar but clearly different lattice yielding extra reflections forbidden by the Jeffery lattice. Clinker alites consistent (presumably impurity stabilised) with this high-temperature polymorph were also found. Some ED features could not be explained by reference to either 'pseudo-twinning' or stabilised high-temperature polymorphs. TEM–ED's of various clinker alites from the work of Groves and Hudson are given in Figs 21(b) and (f). Other microstructural features, such as dislocations and planar defects (see also Figs 21(e) and (f)), including those in clinker C_3A (Fig. 21(e)) have been mentioned in Section 3.3.

4. FUTURE POSSIBILITIES

Much research activity is still being invested into looking for newer cement types and into the behaviour of established cements prepared under novel conditions. As long as this situation persists there will always be a need to relate the properties of the hydrated products to the microstructure of the unhydrated material; this is for reasons of furtherance of both basic understanding and predictive abilities. Although, understandably, most of the effort is aimed at the ongoing hydration process, a clearer understanding of basic relationships, such as between microstructural defects, polymorphism (e.g. of belites), initial hydration rates and strength, is still required. Optical microscopy *per se* is unlikely to reveal new microstructural secrets here; the authors believe that the major advances from electron microscopy and its many related techniques (e.g. FEM/FIM (field emission–ion microscopy); EEM (electron emission microscopy); PSM (proton scattering microscopy); MEM (mirror electron microscopy); SHEED (scanning high-energy electron diffraction); LEED (low-energy electron diffraction)) are more promising. The beginnings of HRTEM (high resolution (transmission) electron microscopy) may be seen in the ion-beam thinning work discussed in Sections 3.3 and 3.4.

This chapter concludes with some rather more conjectural discussions into three possible future avenues for fruitful research into cement microscopy.

4.1. SEM-Associated Techniques

Although the spatial resolution of commercial SEMs has improved dramatically over the last 15 or so years (from 250 Å to 30–50 Å), little appropriation of this improvement is foreseen with studies on unhydrated cement. The case with *hydrated* cement is different since the three-dimensional morphology of early hydration products (sheets, foils, tubes, etc., see Chapter 6) would clearly benefit from improved SEM micrography. Unhydrated cement morphology has, however, long been within the grasp of optics, whereas the required breakthrough in microstructural understanding requires advances in TEM applications rather than in SEM applications. Where the SEM might, however, hold promise is in the fuller exploitation of the emissive signals emanating from the specimen under the raster mode of the scanning electron beam; such exploitations remain well within our definition of microscopy (Section 1). Today, SEM manufacturers offer detectors for most emissive/absorptive modes of operation:

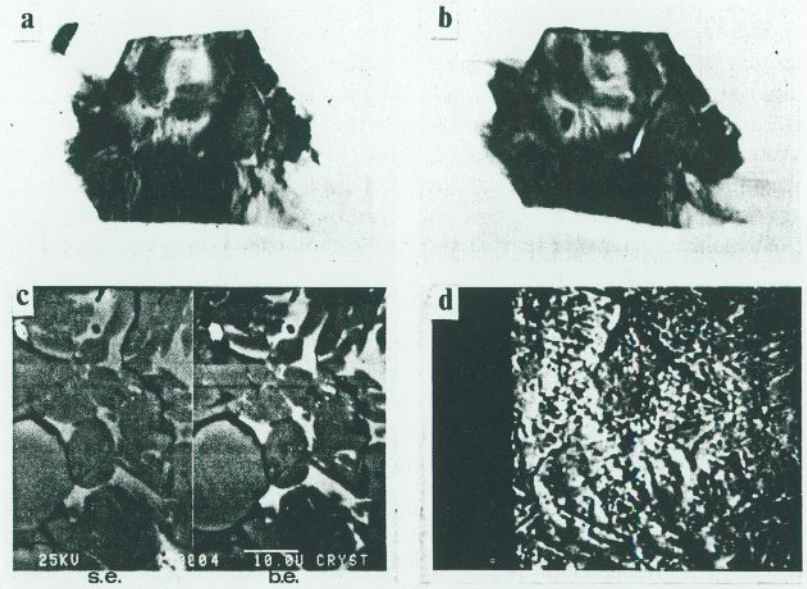

Fig. 22. Examples of other radiative forms of cement microscopy that are now becoming possible: (a) and (b) synchrotron x-ray source topographs[164] (two different reflections) of a synthetic $Ca(OH)_2$ crystal revealing various zone boundaries, at least three major hexagonal growth zones, a misoriented inclusion (clearly displaced in (a)), and heavier defect structure propagating radially in the outer zone; (c) back-scattered electrons—the split screen SEM micrograph of Portland cement[166] compares the atomic number contrast evident with secondary electron (s.e.—left-hand side) and back-scattering electron (b.e.—right-hand side) imaging systems. The latter clearly resolves small atomic number variations with much improved sensitivity; (d) scanning acoustic microscopy (SAM) of compacted Portland cement; this micrograph was taken[167] at 1 GHz with a surface resolution of 1 μm though with this preliminary attempt the detail evident is probably dominated by surface effects arising from the use of etchants which could be avoided with future attempts.

specimen current; back-scattered electron,* Auger electron;** x-ray fluorescence (Section 3.2); electron energy loss spectrometers (EELS); and cathodo-luminescence (CL)† detector-display systems. EELS is usually associated with STEM-†† dedicated machines, whereas Auger-electron and cathodo-luminescence systems are still undergoing technological improvements which may or may not be appropriate for cement-related topics: cathodo-luminescence in particular is capable of offering information on defect and fine-inclusion distributions in mineralogical sections using the more recent efficient optical collector–detectors normally sensitive in the optical range, but extendable into the UV and near IR regions.

SEMs are currently experiencing a much improved energy resolution in back-scattered electron detectors. The potential of the improved energy discrimination (equivalent to as little as 0·2 difference in average atomic weight) lies in the area of microanalysis rather than in electron imaging—see Fig. 22(c). The new back-scattered electron detectors might prove useful for analysing small changes in solid solution in the cement clinker interstitial matrix, although for an absolute analysis the method should be used together with an x-ray fluorescence detector acting as a calibrant.

* Secondary electron detectors are synonymous with the most commonly used and conventional mode of SEM operation. The basic design (termed 'Everhardt–Thornley') is aimed at efficiently trapping electrons ejected from the sample with energies in the 0–50 eV range. Back-scattered electron detectors are normally sensitive over a 2 keV $\rightarrow E_0$ energy range (where E_0 is the incident beam energy, typically 20 keV) which will include characteristic energy bands/absorptions arising from specific electron–host atom interactions.

** Auger electron is the name given to the event in which an inner atom vacancy is filled by an outer electron but with the excess energy being internally transferred to another outer electron. The net result is two outer electron vacancies and an ejected 'Auger electron' possessing an energy characteristic of the transitions involved. Auger-electron currents are very small and difficult to detect, although they are more easily detected with low-atomic-number elements and are associated with a very fine (10–20 Å) spatial resolution.

† Cathodo-luminescence is the SEM mode suitable for materials which emit light under electron bombardment. Such materials are mostly mineral or semiconductor in nature though organic and polymeric examples are evident. The main technology is in the light detection/spectrometer systems designed to efficiently discriminate against accidental electron-scintillation and noise. Apart from analytical purposes, the technique can indicate chemical information (e.g. π-bonding in five- and six-membered rings) and crystal strain. The spatial resolution is inherently close to that for x-ray fluorescence ($\sim\mu$m's) but can, in fact, be much superior (<1000 Å) in cases where the light is strongly self-absorbed by the material.

Regarding x-ray fluorescence detectors, it is felt that SEM microscopy has already experienced the greater part of the EMPA revolution; the introduction of features such as windowless solid-state detectors (for detection of low-atomic-number elements, including C, N and O), more complex combinations with crystal (wavelength dispersive systems) spectrometers and computer-aided automation extends the scope and convenience of microanalysis, but no real conceptual advance is implied. The practice of EMPA in high-performance STEMs could well be further used for determining compositional variations in connection with microstructural studies (Section 3.3). Finally, we should acknowledge the possibility of scanning or microprobe operations other than those based on electron irradiation. Raman microprobe (or molecular optical laser examiner, 'MOLE'), for example, can examine spectra for particles as small as 1 μm, and therefore come within the definition of scanning microscopy. Conjeaud and Bayer[163] have applied the technique to cement alite, belite, C_3A, alumino-ferrites and C-S-H I products. The technique is tuned to symmetric SiO_4 stretching in the 800–900 cm^{-1} range, although the lines are sensitive to the presence of foreign ions (e.g. Fe^{3+}) and possibly crystal size and shape. Figure 22 gives some recent examples by Barnes *et al.*[164,166,167] of newer uses of microscopy on cement sections.

4.2. TEM-Associated Techniques

Examples have already been given (Sections 3.3 and 3.4) of how TEM + ED can yield new information on cement microstructure. This advance can be traced to two main developments: better specimen thinning (ion-beam) and preparative techniques, and the improved performance and availability of HVTEMs. Ultra-high resolution lattice imaging, with or without computer-aided image processing, has yet to be exploited in cement microstructural studies. Already in the area of alumino-silicates, the lattice imaging of many minerals (e.g. ZSM-35 zeolite, serpentine minerals and others as discussed in Chapter 1) is well established; in addition to the resolution of individual crystal defects, such as dislocations, the more complex stacking faults (e.g. multiple-chain planes sandwiched within

†† The term 'STEM' has been largely omitted in this chapter to avoid confusion since, in practice, most cases can still be assigned to a SEM or TEM type operation. Currently, most high-performance TEMs can also operate in a STEM mode thus combining the advantages of the highly developed TEM electron-optics designed for thin specimens with the superior chromatic aberration inherent in SEM mode detection. The combination is particularly appropriate for TEM microanalysis (see Section 3.3).

single or double SiO_4-chain structures) and the distribution of non-stoichiometry through planar mismatching of different groups (e.g. graphite–$FeCl_3$ intercalate) have been evidenced. There are no obvious reasons why cement crystalline phases cannot be subjected to this type of examination. The relationship between defect densities and early-hydration rates, and the role of stabilising impurities in alite and belite has already been mentioned.

As regards ED, one relatively new variation, convergent beam electron diffraction or 'CBED', has been successfully applied to studying metals and alloys. The apparent advantage of the technique lies in its ability to distinguish between very similar lattices, and so it might be appropriate for identification of the close polymorphs of cement alite and belite. The chief skill required is that of intimate familiarisation with the characteristic CBED patterns obtained from the various polymorphs over all configuration space. Examples of some preliminary attempts[129] are given in Fig. 23.

4.3. Other Radiative Devices

In addition to electrons, x-rays have already been mentioned (Section 1) as a potential imaging radiation. X-ray microscopes with spatial resolutions between 100 and 1000 Å are under discussion and are undergoing preliminary trials (see also Fig. 1(IVa)). In the present context, there would appear to be little advantage over existing electron microscopes for looking at crystalline cement phases, but there could be distinct advantages for studying cement hydration. If it were coupled to a high-intensity variable-wavelength x-ray source (i.e. a synchrotron radiation source, 'SRS'), the x-ray microscope would further provide the possibility of performing dynamic hydration experiments *in situ* with the advantages (over electrons) of lesser degradation, better resolution in the aqueous vapour environment, lower beam damage (absorption of x-rays compared to electrons), exposure times of the order of a second, accommodation of variable specimen thickness, and a more stable vapour environment. However, above all, the variable and well-controlled wavelengths of SRS x-rays would permit one to 'tune into' selected absorption edges of the atomic constituents (O, Si, Ca, etc.) of the hydrating products.

X-ray Lang topography has already been mentioned in Section 1, and on this topic we are able to refer to a preliminary study[164] on defects within laboratory-solution-grown $Ca(OH)_2$ ('CH' or 'portlandite') crystals. While the crystal perfection shown is far removed from that normally encountered in near-perfect semi-conductors with typical dislocation

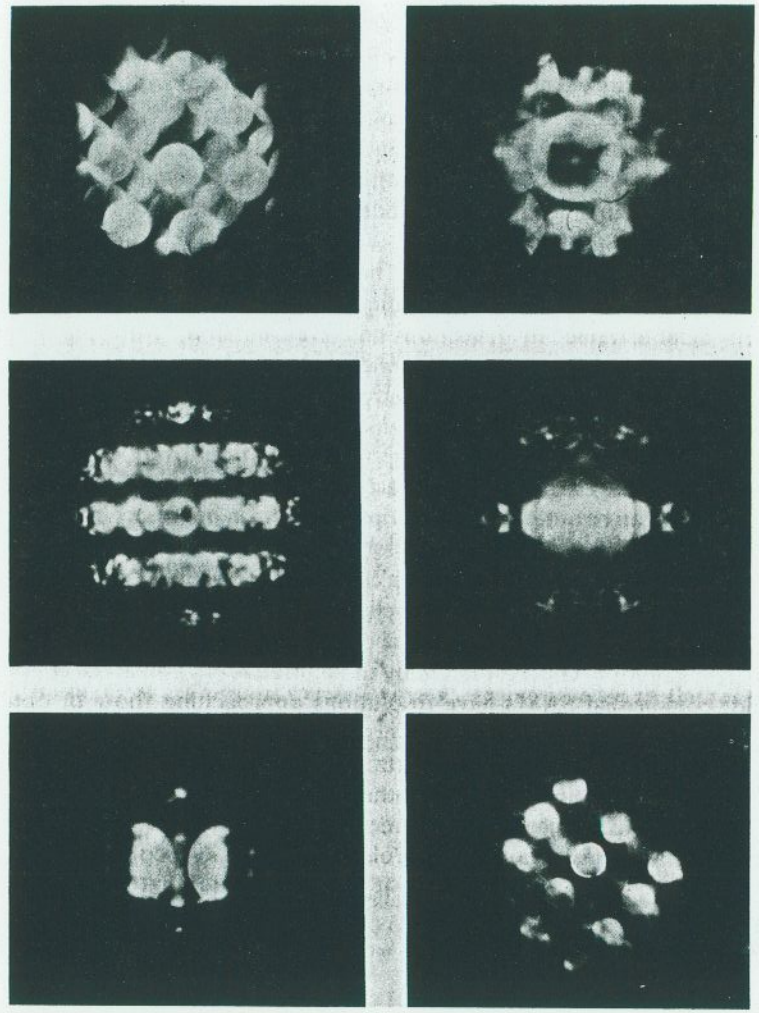

Fig. 23. Some examples of preliminary attempts at the convergent beam electron diffraction (CBED) of β-C_2S crystals at 100 keV (crystal orientations unknown).[129]

densities of around 0 to, say, 100 cm^{-2}, the SERC synchrotron x-ray source (at Daresbury, UK) operating at typical power (2·0 GeV and 50–200 mA beam current) can yield interpretable topographs after some 2–6 min exposure. Figures 22(a) and (b) show an example of x-ray topographs from a CH crystal in which growth sector boundaries are visible as well as dislocations structures propagating out in a radial direction. The technique is admittedly far more appropriate to macroscopic (≥ 1 mm) crystals than typical cement crystallites ($\leq 100\ \mu m$), but can be usefully used for studying details of growth modes in larger model crystals that might be later related to actual cementitious structures.

Microscopy need not necessarily be restricted to electrons and x-rays. Acoustic microscopy[165] (or scanning acoustic microscopy (SAM)) has been demonstrated in reflection and transmission, with phase and amplitude detectors, and using sonic input with frequencies up to the gigahertz range. Obvious practical advantages are that the signals detected are easily digitised for computer-aided image analysis (elasticity, density, velocity-maps, etc.) and that spherical aberration is intrinsically low compared to diffraction. The contrast produced is a 'mechanical contrast' and as such can be quite different to optical/electron microscope contrast—an effect well suited to biological tissues where the tedious and uncertain practice of heavy-atom staining for electron microscopy is obviated with the SAM. The SAM contrast is well suited for non-destructive internal bond testing or crack detection. One of the main limitations is the current spatial resolution which is limited by the sound absorption in the coupling fluid; commercial SAMs have resolutions approaching those of optical microscopes although more exotic versions (e.g. hot-water or high-pressure coupling media, higher megahertz frequency range) may push the resolution to below 1000 Å. Whether SAM might be useful for such inhomogeneous structures as cement, or whether less conventional radiation devices generally have a role in cement microscopy, is presently far from obvious, and therefore it is appropriate that we close this speculative section at this point.

ACKNOWLEDGEMENTS

We wish to acknowledge the research support of various funding agencies (Cement Makers' Federation, Science and Engineering Research Council, Blue Circle Industries PLC), and facilities/materials offered by JEOL Ltd, CACA (Slough), and the Imperial College High Voltage TEM. For various contributions we thank Professor J. W. Jeffery, Dr S. Chatterji, Dr A. L. Mackay, Dr A. P. Barker, Mr S. E. Tarling, Mr G. Fisher, Mr N. T. Moore and Mrs N. Nicholas (Birkbeck College), Dr G. Bye, Mr P. Hines, Dr I. Smith (Blue Circle), Dr C. H. Fentiman (Lafarge Aluminous Cement Co.), Professor H. F. W. Taylor and Dr A. Gard for EM facilities at Aberdeen University, and Professor J. F. Young and Mr S. Chopra (University of Urbana). The photographic reproductions were done by Mr Packer and Mrs S. M. Tench.

REFERENCES

1. LANG, A. R., *Acta Cryst.*, **12**, 249 (1959).
2. BARRETT, C. S., *Trans. Am. Inst. Mech. Eng.*, **161**, 15 (1945).
3. LE CHATELIER, H., *Experimental Researches on the Constitution of Hydraulic Mortars*, (translated by J. L. Mack), McGraw-Hill, New York (1905).
4. (a). TORNEBOHM, A. E., *Tonid-Ztg.*, **21**, 1148 (1897); (b). TORNEBOHM, A. E., *Baumaterialienhunde*, **6**, 142 (1910–11); (c). TORNEBOHM, A. E., *Zement*, **4**, 287 (1903).
5. (a). MAKI, I. and CHROMY, S., *Cem. Concr. Res.*, **8**(4), 407 (1978); (b). MAKI, I. and CHROMY, S., *Il Cemento*, **75**, 247 (1978).
6. HARTSHORNE, N. H. and STUART, A., *Crystals and the Polarising Microscope*, Edward Arnold and Co., London (1934).
7. ROGERS, A. F. and KERR, P. F., *Optical Mineralogy*, McGraw-Hill, New York (3rd edn.) (1942).
8. BUNN, C. W., *Chemical Crystallography: An Introduction to Optical and X-ray Methods*, Clarendon Press, Oxford (2nd edn.) (1961).
9. WAHLSTROM, E. E., *Optical Crystallography*, (2nd edn.), John Wiley & Sons Inc., New York (1951).
10. NYE, J. F., *Physical Properties of Crystals*, Clarendon Press, Oxford (1957).
11. (a). DORN, J. D., *Proc. 4th Int. Conf. Cement Microscopy*, Las Vegas, 178 (1982); (b). WERNER, R. L., *Proc. 4th Int. Conf. Cement Microscopy*, Las Vegas, 225 (1982).
12. (a). BOGUE, R. H., *The Chemistry of Portland Cement*, Reinhold Publishing Corporation, New York (2nd edn.) (1955); (b). INSLEY, H. and FRECHETTE, V. D., *Microscopy of Ceramics and Cements*, Academic Press, New York (1955).
13. MIDGLEY, H. G. and TAYLOR, H. F. W., In: *The Chemistry of Cements*, H. F. W. Taylor (ed.), Academic Press, London/New York, Vol. 2 (1964), p. 223.
14. LEA, F. M., In: *The Chemistry of Cement and Concrete*, Edward Arnold Ltd., London (3rd edn.) (1970), p. 91.
15. AHMED, W. U., *Proc. 3rd. Int. Conf. Cement Microscopy*, Houston (1981), p. 1.

16. (a). CHOPRA, S. K., NARANG, K. C., GHOSH, S. P. and SHARMA, K. M., *Proc. 7th Int. Cong. Chem. Cement*, Paris, **III** (1980), p. VII–51; (b). DREIZLER, I. E., *Proc. 3rd Int. Conf. Cement Microscopy*, Houston (1981), p. 33; (c) GOUDA, G. R. and BAYLES, J., *Proc. 3rd Int. Conf. Cement Microscopy*, Las Vegas (1981), p. 89; (d). NARANG, K. C., GHOSH, S. P. and SHARMA, K. M., *Proc. 3rd Int. Conf. Cement Microscopy*, Las Vegas (1981), p. 140.
17. MAKI, I. and GOTO, K., *Cem. Concr. Res.*, **12**(3), 301 (1982).
18. (a). MAKI, I. and KATO, K., *Cem. Concr. Res.*, **12**(1), 93 (1982); (b). CHROMY, S. and MAKI, I., *Cem. Concr. Res.*, **12**(4), 511 (1982); (c). MAKI, I., *Il Cemento*, **76**, 167 (1979).
19. BOIKOVA, A., *Proc. 7th Int. Cong. Chem. Cement*, Paris, **II** (1980), p. I–6.
20. ONO, Y., *Proc. 3rd Int. Conf. Cement Microscopy*, Las Vegas (1981), p. 198.
21. (a). ONO, Y., KAWAMURA, S. and SODA, Y., *Proc. 5th Int. Cong. Chem. Cement*, Tokyo, **I** (1968), p. 275; (b). see, for example, Reference 113.
22. (a). ONO, Y., *Proc. 7th Int. Cong. Chem. Cement*, Paris, **II** (1980), p. I–206; (b). ONO, Y., *Microscopic Analysis of Clinkers*, report of the Central Research Laboratory, Onoda Cement Co. (1973); (c). ONO, Y., *Microscopic Analysis of Clinkers*, report of the Central Research Laboratory, Onoda Cement Co. (1975).
23. CHROMY, S., *J. Am. Ceram. Soc.*, **50**, 677 (1967).
24. GREEN, K. T., *J. Res. Natl. Bur. Standards*, **32**, 1 (1944).
25. RANKIN, G. A., *Am. J. Sci.*, **39**, 1 (1915).
26. (a). MAKI, I., *Cem. Concr. Res.*, **6**(6), 797 (1976); (b). MAKI, I., *Cem. Concr. Res.*, **6**(2), 183 (1976).
27. (a). MAKI, I., *Cem. Concr. Res.*, **3**(3), 295 (1973); (b). MAKI, I., *Cem. Concr. Res.*, **4**(1), 87 (1974).
28. BARNES, P., FENTIMAN, C. H. and JEFFERY, J. W., *Acta Cryst.*, **A36**, 353 (1980).
29. (a). INSLEY, H., *J. Res. Natl. Bur. Standards*, **17**, 353 (1936); (b). INSLEY, H. and MCMURDIE, H. F., *J. Res. Natl. Bur. Standards*, **20**, 173 (1938); (c). INSLEY, H., *J. Res. Natl. Bur. Standards*, **25**, 295 (1940).
30. MILLER, T., *Proc. 3rd Int. Conf. Cement Microscopy*, Houston (1981), p. 56.
31. VARMA, S. P. and WALL, C. D., *Cem. Concr. Res.*, **11**(4), 567 (1981).
32. CHATERJEE, A. K., *World Cem. Tech.*, **10**(4), 124 (1979).
33. WHITE, A. H., *Ind. Eng. Chem.*, **1**, 5 (1909).
34. CHATERJEE, A. K., *World Cem. Tech.*, **10**(5), 165 (1979).
35. JEFFERY, J. W., *Acta Cryst.*, **5**, 26 (1952).
36. GUINIER, A. and REGOURD, M., *Proc. 5th Int. Cong. Chem. Cement*, Tokyo, **I** (1968), p. 1.
37. GUTTMAN, A. and GILLE, F., *Zement*, **17**, 296 (1928).
38. YAMAGUCHI, G. and TAKAGI, S., *Proc. 5th Int. Cong. Chem. Cement*, Tokyo, **I** (1968), p. 181.
39. JELENIC, I., BEZJAK, A. and BUJAN, M., *Cem. Concr. Res.*, **8**(2), 173 (1978).
40. GHOSE, A. and BARNES, P., *World Cem. Tech.*, **12**(1), 37 (1981).
41. (a). HUDSON, K. E. and GROVES, G. W., *Cem. Concr. Res.*, **12**(1), 61 (1982); (b). GROVES, G. W., *J. Mater. Sci.*, **16**, 1063 (1981); (c). GROVES, G. W., *Cem. Concr. Res.*, **12**(5), 619 (1982).
42. BENSTED, J., *Cem. Conc. Res.*, **8**(1), 73 (1978).
43. MAYCOCK, J. N. and MCCARTY, M., JR., *Cem. Concr. Res.*, **3**(6), 701 (1973).

44. PRITTS, I. M. and DAUGHERTY, K. E., *Cem. Concr. Res.*, **6**(6), 783 (1976).
45. BENSTED, J., *Cem. Concr. Res.*, **9**(1), 97 (1979).
46. GHOSH, S. N. and HANDOO, S. K., *Cem. Concr. Res.*, **10**(6), 771 (1980).
47. JELENIC, I. and BEZJAK, A., *Cem. Concr. Res.*, **11**(3), 467 (1981).
48. CHATERJEE, A. K. and GHOSH, S. N., *World Chem. Tech.*, **11**(5), 252 (1980).
49. KAZANSKAIA, A. N. and SYTCHEV, M. M., *Proc. 7th Int. Cong. Chem. Cement*, Paris, **IV** (1980), p. 275.
50. SUZUKI, K., *Proc. 7th Int. Cong. Chem. Cement*, Paris, **II** (1980), p. II–47.
51. MATKOVIC, B., CARIN, V., GACESA, T. and HALLE, R., *Proc. 7th Int. Cong. Chem. Cement*, Paris, **II** (1980), p. I–189.
52. BOIKOVA, A. I., DEGEN, M. G. and PARAMONOVA, V. A., *Proc. 6th Int. Cong. Chem. Cement*, Moscow, **I** (1976), p. 68.
53. GHOSH, S. N., RAO, P. B., PAUL, A. K. and RAINA, K., *J. Mater. Sci.*, **14**, 1554 (1979).
54. LEHMANN, H., TRANSTEL, S. and JACOB, P., *Tonind-Ztg. Keram. Rdsh.*, **86**, 316 (1962).
55. NARJES, A., *Zement–Kalke–Gips*, **12**, 129 (1959).
56. WELCH, J. H. and GUTT, W., *Proc. 4th Int. Cong. Chem. Cement*, Washington, **I** (1960), p. 59.
57. GUTT, W. and OSBORN, E. F., *Cem. Tech.*, **1**(4), 121 (1970).
58. REGOURD, M. and GUINIER, A., *Proc. 6th Int. Cong. Chem. Cement*, Moscow, **I** (1974), p. 25.
59. GHOSH, S. N. and CHATERJEE, A. K., *J. Mater. Sci.*, **9**, 1577 (1974).
60. MONDAL, P. and JEFFERY, J. W., *Acta Cryst.*, **B31**, 689 (1975).
61. (a). HAN, K. S., GARD, J. A. and GLASSER, F. P., *Cem. Concr. Res.*, **11**(1), 79 (1981); (b). LEE, F. C., BANDA, H. M. and GLASSER, F. P., *Cem. Concr. Res.*, **12**(2), 237 (1982); (c). TAKEUCHI, Y., NISHI, F. and MAKI, I., *Zeitschrift für Krist.*, **152**, 259 (1980); (d). VARMA, S. P., HENDERSON, E. and WALL, C. D., *Cem. Concr. Res.*, **11**(2), 211 (1981).
62. (a). REGOURD, M., CHROMY, S., HJORTH, L., MORTUREUX, B. and GUINIER, A., *Rev. Mat. Constr.*, **682**, 7 (1973); (b) REGOURD, M., *Il Cemento*, **3**, 323 (1978).
63. VARMA, S. P. and WALL, C. D., *Cem. Concr. Res.*, **11**(4), 567 (1981).
64. ONO, Y. and SHIMODA, T., *Semento Gijutsu Nenpo*, **XXI**, 30 (1967).
65. TIMASHEV, V. V., *Proc. 7th Int. Cong. Chem. Cem.*, Paris, **I** (1980), p. I–3/1.
66. SKALNY, J. and YOUNG, J. F., *Proc. 7th Int. Cong. Chem. Cem.*, Paris, **I** (1980), p. II–1/3.
67. OPOCZKY, L. and JUHASZ, Z., *Proc. 6th Int. Cong. Chem. Cem.*, Moscow, **II**(1) (1974), p. 173.
68. TIMASHEV, V. V. and AKIMOV, V. G., *Proc. 7th Int. Cong. Chem. Cem.*, Paris, **IV** (1980), p. 203.
69. DESCAMPS, J., FIERENS, P. and VERHAEGEN, J. P., *Proc. 6th Int. Cong. Chem. Cem.*, Moscow, **II** (1974), p. 143.
70. SAKURAI, T., SATO, T. and YOSHINAGA, A., *Proc. 5th Int. Cong. Chem. Cem.* Tokyo, **I** (1968), p. 300.
71. MAYCOCK, J. N., SKALNY, J. and KALYONCU, R., *Cem. Concr. Res.*, **4**(5), 835 (1974).

72. FIERENS, P. and VERHAEGEN, J. P., *Cem. Concr. Res.*, **5**(3), 233 (1975).
73. FIERENS, P. and VERHAEGEN, J. P., *Cem. Concr. Res.*, **5**(6), 587 (1975).
74. FIERENS, P., VERHAEGEN, A. and VERHAEGEN, J. P., *Cem. Concr. Res.*, **4**(4), 381 (1974).
75. FIERENS, P. and VERHAEGEN, J. P., *Cem. Concr. Res.*, **6**(1), 103 (1976).
76. ONO, Y. and SODA, Y., *Semento Gijutsu Nenpo*, **19**, 93 (1965).
77. ORDWAY, F., *Proc. 4th Int. Cong. Chem. Cement*, Washington, **I** (1960), p. 39.
78. SPRUNG, S., *Proc. 7th Int. Cong. Chem. Cem.*, Paris, **I** (1980), p. I–2/1.
79. PROUT, W. J., *Proc. 4th Int. Conf. Cem. Microscopy*, Las Vegas (1982), p. 2.
80. CHEN, H., *Proc. 4th Int. Conf. Cem. Microscopy*, Las Vegas (1982), p. 4.
81. HAWKINS, P., *Proc. 4th Int. Conf. Cem. Microscopy*, Las Vegas (1982), p. 6.
82. CAMPBELL, D. H., *Proc. 4th Int. Conf. Cem. Microscopy*, Las Vegas (1982), p. 7.
83. O'NEILL, R. C., *Proc. 4th Int. Conf. Cem. Microscopy*, Las Vegas (1982), p. 9.
84. WHEELER, O. N., JR., *Proc. 3rd Int. Conf. Cem. Microscopy*, Houston (1981), p. 171.
85. MILLER, F. M., *Proc. 3rd Int. Conf. Cem. Microscopy*, Houston (1981), p. 181.
86. ST. JOHN, D. A. and MCGAVIN, P. N., *Proc. 3rd Int. Conf. Cem. Microscopy*, Houston (1981), p. 193.
87. (a). HARGRAVE, R. V., SHAH, R. D., CHATTERJEE, A. K. and RANGNEKAR, *Proc. 4th Int. Conf. Cem. Microscopy*, Las Vegas (1982), p. 110; (b). FUNDAL, E., *World Cem. Tech.*, **10**(6), 195 (1979); (c). HARGRAVE, R. V., VENKAKESWARAN, D., CHATTERJEE, A. K. and RANGNEKAR, B. S., *Proc. 5th Int. Conf. Cem. Microscopy*, Nashville (1983).
88. (a). HICKS, J. K. and DORN, J. D., *Proc. 4th Int. Conf. Cem. Microscopy*, Las Vegas (1982), p. 83; (b). LONG, G. R., *Proc. 4th Int. Conf. Cem. Microscopy*, Las Vegas (1982), p. 92.
89. DORN, J. D., *Cem. Concr. Res.*, **8**(5), 635 (1978).
90. (a). DREIZLER, I. E., *Proc. 4th Int. Conf. Cem. Microscopy*, Las Vegas (1982), p. 50; (b). JANKO, A., *Proc. 4th Int. Conf. Cem. Microscopy*, Las Vegas (1982), p. 67; (c). LONG, G. R., *Proc. 4th Int. Conf. Cem. Microscopy*, Las Vegas (1982), p. 128; (d). WIEJA, C. and WIEJA, K., *Proc. 4th Int. Conf. Cem. Microscopy*, Las Vegas (1982), p. 141.
91. KAY, D., *Techniques for Electron Microscopy*, Blackwell Scientific Publishers Ltd, Oxford (2nd edn.) (1967).
92. GOODHEW, P. J., *Electron Microscopy and Analysis*, Wykeham Publications Ltd, London (1975).
93. SIEGEL, B. M. and BEAMAN, D. R., *Physical Aspects of Electron Microscopy and Microbeam Analysis*, John Wiley and Sons, London (1975).
94. GRUNDY, P. J. and JONES, G. A., *Electron Microscopy in the Study of Materials*, Edward Arnold, London (1976).
95. A series of several volumes on all aspects of Electron Microscopy, edited by A. M. Glauert, Elsevier North-Holland Publishing Co., Amsterdam and New York.
96. GARD, J. A., In: *The Chemistry of Cements*, Vol. 2, H. F. W. Taylor (ed.), Academic Press, London and New York (1964).
97. GARD, J. A., *The Electron Optical Investigation of Clays*, J. A. Gard (ed.), The Mineralogical Society, London (1971).

98. DELOYE, F. X. and LOUARN, N., *Compt. Rend. Hebd. Seances Acad. Sci., Ser. D.*, **279**(9), 707 (1974).
99. HIRSCH, P. B., HOWIE, A., NICHOLSON, R. B., PASHLEY, D. W. and WHELAN, M. J., *Electron Microscopy of Thin Crystals*, Butterworths, London (1967).
100. PHILLIPS, V. A., *Modern Metallographic Techniques and Their Applications*, Wiley-Interscience, New York (1971).
101. HREN, J. J., GOLDSTEIN, J. I. and JOY, D. C. (eds.), *Introduction to Analytical Electron Microscopy*, Plenum Press, New York (1979).
102. GOLDSTEIN, J. I. and YAKOWITZ, H. (eds.), *Practical Scanning Electron Microscopy*, Plenum Press, New York (1975).
103. YAMAGUCHI, G. and TAKAGI, S., Present-Day Methods of Investigation of the Clinker Formation Mechanism and Clinker Phase Composition. Principal paper, session I-1, *Proc. 6th Int. Cong. Chem. Cements*, Moscow, 1974.
104. SKALNY, J., MANDER, J. E. and MEYERHOFF, M. H., *Cem. Concr. Res.*, **5**(2), 119 (1975).
105. MANDER, J. E. and SKALNY, J. P., *Bull. Am. Ceram. Soc.*, **56**(11), 987 (1977).
106. WOJNAROVITS, L. and UDVARDI, M., *Epitoanyag*, **28**(5), 162 (1976).
107. GOUDA, G. R., *Proc. 7th Int. Cong. Chem. Cements*, Paris, Vol. 2 (1980), p. I–235.
108. GOUDA, G. R., *Proc. 3rd Int. Conf. Cement Microscopy*, Houston (1981), p. 127.
109. BAYLES, J. and GOUDA, G. R., Ibid., p. 106.
110. HORNAIN, H. and REGOURD, M., *Proc. 7th Int. Cong. Chem. Cements*, Paris Vol. 2 (1980), p. I–276.
111. BARNES, P., FONSEKA, G. M., GHOSE, A. and MOORE, N. T., *J. Mater Sci.*, **14**(12), 2831 (1979).
112. GHOSE, A. and BARNES, P., *Indian Concrete J.*, **55**(9), 255 (1981).
113. MATKOVIC, B. *et al.*, *Bull. Am. Ceram. Soc.*, **60**(8), 825 (1981).
114. BOBESIC, B., HALLE, R., MIKOC, M., MATKOVIC, B. and YOUNG, J. F., *Bull. Am. Ceram. Soc.*, **60**(11), 1164 (1981).
115. CHATTERJEE, S., *Cement Technology*, **6**(1), 5 (1975).
116. GRATTAN-BELLOW, P. E., QUINN, E. G. and SEREDA, P., *J. Cem. Concr. Res.*, **8**(3), 333 (1978).
117. (a). BEAMAN, D. R. and ISASI, J. A., *Rev. Mat. Res. Stand.*, **11**(11), 8; **11**(12), 12 (1971); (b). KOVACS, K. and TAMAS, F., *Proc. 4th Int. Conf. Cement Microscopy*, Las Vegas (1982), p. 156.
118. HOLT, D. B., MUIR, M. D., GRANT, P. R. and BOSWARVA, I. M., *Quantitative Scanning Electron Microscopy*, Academic Press, London (1974).
119. MIDGLEY, H. G., *Mag. Concr. Res.*, **20**(62), 41 (1968).
120. MIDGLEY, H. G., *Proc. 5th Int. Symp. Chem. Cem.*, Tokyo, Vol. 1 (1968), p. 226.
121. FLETCHER, K. E., *Mag. Concr. Res.*, **20**(64), 167 (1968).
122. FLETCHER, K. E., *Mag. Concr. Res.*, **21**(66), 3 (1969).
123. BLUM, F. and BRANDT, M. P., *X-ray Spectrometry*, **2**, 121 (1973).
124. RUSS, J. C., *9th Annual Conf. of the Microbeam Analysis Society*, Canada (1974).
125. MOORE, N. T., SARKAR, S. L. and JEFFERY, J. W., *World Cement Technology*, **8**(6), 240 (1977).
126. BARNES, P., JEFFERY, J. W. and SARKAR, S. L., *Cem. Concr. Res.*, **8**, 559 (1978).

127. SARKAR, S. L., *Indian Concrete J.*, **52**(2), 55 (1978).
128. GHOSE, A. and BARNES, P., *Cem. Concr. Res.*, **9**(6), 747 (1979).
129. GHOSE, A., PhD Thesis, University of London (1980).
130. RUSS, J. C., *ASTM Special Technical Publication*, **485**, 154 (1970).
131. SOLOSKY, L. F. and BEAMAN, D. R., *Rev. Sci. Instr.*, **43**(8), 1100 (1972).
132. DIAMOND, S., *Cem. Concr. Res.*, **2**(5), 617 (1972).
133. DIAMOND, S., YOUNG, J. F. and LAWRENCE, F. V., JR., *Cem. Concr. Res.*, **4**(6), 899 (1974).
134. MOORE, A. E., *Silicates Industriels*, **30**(8), 445 (1965).
135. PETERSON, O., *Zement-Kalk-Gips*, **20**(2), 61 (1967).
136. MIDGLEY, H. G., In: *The Chemistry of Cements, Volume 1*, H. F. W. Taylor (ed.), Academic Press, London (1964), p. 89.
137. MIDGLEY, H. G. and BENNETT, M., *Cem. Concr. Res.*, **1**(4), 413 (1971).
138. REGOURD, M. and GUINIER, A., *Proc. 6th. Int. Cong. Chem. Cements*, Moscow (1974).
139. HORNAIN, H., *Rev. Mater. Constr.*, **680**, 4 (1973).
140. KRISTMANN, M., *Cem. Concr. Res.*, **8**(1), 93 (1978).
141. GHOSE, A. and BARNES, P., *World Cem. Technol.*, **11**(9), 441 (1980).
142. GHOSE, A. and BARNES, P., *J. Am. Ceram. Soc.*, **64**(9), C 120 (1981).
143. EVANS, R. C., *An Introduction to Crystal Chemistry*, Cambridge University Press, Cambridge (1964).
144. TARTE, P., *Nature*, **207**(5000), 973 (1965).
145. MOHAN, K. and GLASSER, F. P., *Cem. Concr. Res.*, **7**, 1; 269; 379 (1977).
146. LEHMAN, H., LOCHER, F. W. and THORMANN, P., *Tonindustrie Zeitung Und Keramische Rundschau*, **88**(21), 489 (1964); **88**(23), 537 (1964).
147. HALE, K. F. and HENDERSON BROWN, M., In: *Structure, Solid Mechanics and Engineering Design*, Part 1, M. Te'eni (ed.), Wiley-Interscience, London (1971).
148. BOIKOVA, A. I., DEGEN, M. G. and PARAMONOVA, V. A., *Proc. 6th. Int. Cong. Chem. Cements*, Moscow (1974).
149. PAPIASHVILI, U. I., YUDOVISH, B. E. and MALININ, YU. S., *Mater. Uses, Conf. Electron, Microsc.*, 9th (1973), p. 315; *Chem. Abst.*, **86**, 20991c (1977).
150. VASILEVA, K. V., TIMASHEV, V. V., ANIKEEVA, T. V. and PAPIASHVILI, U. I., *Tr. Mosk. Khim. Tekhnol. Inst.*, **82**, 100 (1974); *Ceram. Abst.*, **56**(3/4), 52 (1977).
151. VASILEVA, K. V., TIMASHEV, V. V. and ANIKEEVA, T. V., *Tr. Mosk. Khim-Tekhnol. Inst.*, **76**, 135 (1973).
152. GHOSE, A., Unpublished results (1982).
153. GHOSE, A., CHOPRA, S. and YOUNG, J. F., *J. Mater. Sci.* (In Press).
154. CHOPRA, S., MSc Thesis, University of Illinois, Urbana (1982).
155. GEVERS, R., VAN LANDUYT, J. and AMELINCKX, S., *Phys. Stat. Sql.*, **11**, 689 (1965).
156. DENT GLASSER, L. S., LACHOWSKI, E. E., MOHAN, K. and TAYLOR, H. F. W., *Cem. Concr. Res.*, **8**, 733 (1978).
157. LACHOWSKI, E. E., MOHAN, K., TAYLOR, H. F. W. and MOORE, A. E., *J. Am. Ceram. Soc.*, **63**, 447 (1980).
158. POOLEY, F. D., *Phil. Trans. Roy. Soc., London*, **A286**, 625 (1977).
159. RUSS, J. C., *X-ray Spectrometry*, **2**, 11 (1973).

160. LORIMER, G. W., NASIR, M. J., NICHOLSON, R. B., NUTTALL, K., WARD, D. E. and WEBB, J. R., In: *Electron Microscopy and Structure of Materials*,, G. Thomas, R. M. Fulrath and R. M. Fisher (eds.), University of California Press, Berkeley (1971), p. 222.
161. GHOSE, A. and BARNES, P., *Cement* (*Bombay*), **15**(1), 15 (1981).
162. JEFFERY, J. W., Private communication (1982).
163. CONJEAUD, M. and BAYER, H., *Cem. Concr. Res.*, **10**(1), 61 (1980).
164. BARNES, P., BARKER, A. P. and FISHER, G., Unpublished results (1982).
165. SINCLAIR, D. A., SMITH, I. R. and WICKRAMASINGHE, H. K., *The Radio and Electronics Engineer*, **52**(10), 479 (1982).
166. BARNES, P. and BARKER, A. P., Unpublished results (1982/3).
167. BARKER, A. P., BARNES, P., MACKAY, A. L. and WICKRAMASINGHE, H. K., Unpublished results (1983).